ELSEVIER

Contents lists available at ScienceDirect

Ore Geology Reviews

journal homepage: www.elsevier.com/locate/oregeorev





Orogenic gold ores in three-dimensions: A case study of distinct mineralization styles at the world-class Cuiabá deposit, Brazil, using high-resolution X-ray computed tomography on gold particles

Marília Ferraz da Costa ^{a,*}, J. Richard Kyle ^b, Lydia M. Lobato ^a, Richard A. Ketcham ^b, Rosaline C. Figueiredo e Silva ^a, Raphael C. Fernandes ^c

- ^a Programa de Pós-graduação em Geologia, Instituto de Geociências, Universidade Federal de Minas Gerais, Belo Horizonte, Brasil
- ^b Jackson School of Geosciences, The University of Texas at Austin, Austin, United States
- ^c AngloGold Ashanti Córrego do Sítio Mineração S/A, Mina Cuiabá, Sabará, Brazil

ARTICLE INFO

Keywords:
Quadrilátero Ferrífero
Cuiabá
Archean
Orogenic gold
X-ray computed tomography
Ore characterization
Ore processing

ABSTRACT

Ore studies using conventional petrographic methods have an intrinsic limitation that spatial (three-dimensional, 3-D) distribution, orientation, shape and mineral associations have to be inferred by 2-D observations and measurements. Further, developing statistically significant data sets is particularly difficult for gold ores, given the fine grain size and low gold abundance even in high-grade ores. We use high-resolution X-ray computed tomography (HRXCT) and improved processing methods to provide 3-D data of ore textures and in-situ gold particles to discern mineralization styles and improve ore recovery. This is a case study of the Archean, world-class Cuiabá orogenic gold deposit in the Quadrilátero Ferrífero province, the largest underground mine in Brazil.

Selected samples represent distinct mineralization styles at the Cuiabá mine: BIF-hosted ore from the Fonte Grande Sul (FGS) orebody, and gold-bearing quartz-carbonate veins hosted in a metamafic unit from the Veio de Quartzo (VQZ) orebody. This study characterizes shape, size, orientation and mineral associations of over 16,000 gold particles. Segmentation and quantitative measurements of gold particles are particularly challenging due to their small grain size. This issue is addressed using the recently formalized partial volume and blurring (PVB) method. Gold mineralization styles differ in 3-D textural and quantitative aspects including size and spatial distribution. Analysis of the VQZ sample shows that gold particles are mainly free in the quartz-carbonate matrix, with many particles in direct contact with a diverse sulfide mineral assemblage. Gold particles in the BIF-hosted FGS ore form bands in association with high pyrrhotite zones within iron carbonate-rich bands. PVB analysis show that the long axis of measured particles in both ore types ranges from \sim 25 μ m to 1.4 mm, with median values around 115 μ m. Larger particles dominantly are sub-equant to prolate spheroids, with smaller particles appearing to be dominantly sub-equant to equant grains. The HRXCT data reveal that the kinematic processes affect gold shape and orientation and indicate the influence of deformation at the grain scale.

1. Introduction

Conventional petrographic studies on ore materials commonly rely on two-dimensional (2-D) polished thin sections, using techniques such as optical microscopy, scanning electron microscopy (SEM), mineral liberation analysis (MLA) SEM, electron microprobe (EMP) and laser ablation-induced couple plasma-mass spectrometry (LA-ICP-MS). All of these methods have an intrinsic spatial limitation that leads to restricted interpretation of textural relationships, mineral sizes and abundances, as

three-dimensional (3-D) aspects must be inferred from 2-D observations and data from different sections.

High-resolution X-ray computed tomography (HRXCT) is a non-destructive technique that not only provides striking three-dimensional images, but allows in-situ, three-dimensional mineralogical and textural quantifications. The technique has been applied to a variety of geological investigations over the past two decades (e.g. Ketcham and Carlson, 2001; Mees et al., 2003; Cnudde and Boone, 2013), including metamorphic (e.g. Denison and Carlson, 1997;

E-mail address: mariliaferrazc@gmail.com (M. Ferraz da Costa).

https://doi.org/10.1016/j.oregeorev.2021.104584

Received 1 April 2021; Received in revised form 19 October 2021; Accepted 11 November 2021 Available online 18 November 2021

^{*} Corresponding author.

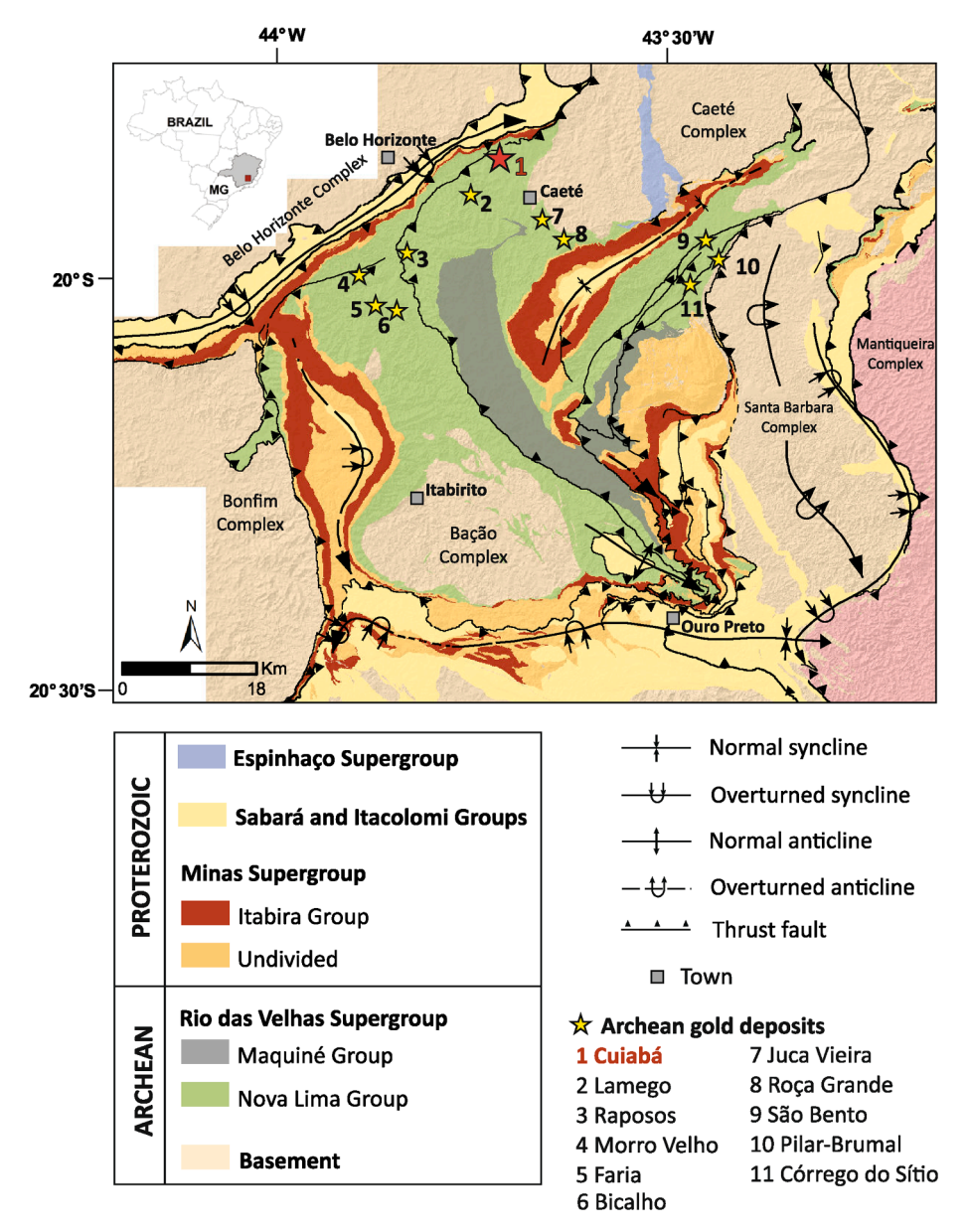


Fig. 1. Simplified geological and structural map of the Quadrilátero Ferrífero region with the main stratigraphic units (based on Dorr, 1969; Baltazar and Zucchetti, 2007; Endo et al., 2019a) and location of major Archean gold deposits (Lobato et al., 2001a).

Huddlestone-Holmes and Ketcham, 2010; Denison et al., 1997; Sayab et al., 2016) and igneous petrography (e.g. Jerram et al., 2009, 2010; Godel et al., 2013a; Vukmanovic et al., 2013); meteoritics (e.g. Hezel et al., 2013, Hanna and Ketcham 2017) and petroleum engineering (e.g. Van Geet et al., 2000; Akin and Kovscek, 2003).

The application of HRXCT to economic geology is remarkably effective in the study of metallic ores, particularly precious metalbearing minerals that typically have significant contrast even with common metallic phases (Kyle and Ketcham, 2015). More recently, HRXCT has been increasingly used as means to investigate ore samples, mainly gold (e.g. Kyle and Ketcham, 2003; Mote et al., 2005; Mauk et al., 2006; Kyle et al., 2008; Wright, 2017), including samples from an orogenic deposit (e.g. Sayab et al. 2016), and PGE ores (e.g. Godel et al., 2006, 2010; Godel, 2013), as well as Fe-Ti-V oxide (Liu et al., 2014), copper (Merinero et al., 2019), and tungsten ores (Le Roux et al., 2015). Furthermore, X-ray CT provides crucial 3-D parameters required for mineral processing (e.g. Miller et al., 2003, 2009; Dhawan et al., 2012; Reyes et al., 2017). Accurate 3-D measurement of size, shape, and orientation, however, can require specialized processing when

economic particles are small relative to the sample volume scanned (Ketcham and Mote, 2019), as is typical when studying precious metal deposits where ore concentrations are only a few grams per tonne.

In this study, samples from the world-class Cuiabá orogenic gold deposit, Brazil (e.g. Lobato et al., 2001a) were selected to represent common mineralization styles recognized in orogenic gold deposits worldwide (e.g., Phillips et al., 1984; Groves et al., 1998; Goldfarb and Groves, 2015). These encompass shear-related, quartz-carbonate veins hosted in metavolcanic rocks (Vitorino et al., 2020) and sulfide-associated, stratabound-style ore in banded iron formation (BIF).

The Cuiabá deposit is located in the Quadrilátero Ferrífero metallogenetic province (Fig. 1) and is the largest active underground mine in Brazil, with 20 levels extending to 1.4 km below surface. The 2019 ore reserves amount to 1.31 Moz with a cutoff grade at 6.04 g/t Au with estimated total resources of 5.26 Moz at 7.45 g/t Au (Resources and Reserves Evaluation Report, AngloGold Ashanti, 2019). The orebody is hosted in greenschist facies mafic metavolcanic rocks, BIF, carbonaceous and micaceous phyllites of the Nova Lima Group, Archean Rio das Velhas greenstone belt (Lobato et al., 2001b).

To analyze in-situ, grain-scale key gold characteristics of BIF- and vein-hosted ores, the samples were scanned using HRXCT and complemented by conventional petrographic studies. This contribution also investigates the influence of the deformation history at Cuiabá on particle relationships and mineral orientations, providing data to discern the gold mineralization styles and improve ore recovery.

2. Regional geology

The Quadrilátero Ferrífero (QF) is located in the south-central part of Minas Gerais state, in the southern São Francisco Craton (Almeida, 1967; Dorr, 1969). It is geologically well known for its gold deposits hosted in the Archean Rio das Velhas greenstone belt, as well as its Paleoproterozoic Lake Superior-type BIF-hosted iron deposits. The QF was the most important Brazilian gold-producing area from the early 18th century until the late 1970s (Lobato et al., 2001a, 2020). This province represents an Archean granite-greenstone terrane overlain by Proterozoic supracrustal sequences. Three main units (Dorr, 1969; Marshak and Alkmim, 1989) dominate: the granite-gneiss terranes; the greenstone belt of the Rio das Velhas Supergroup; and the Proterozoic sedimentary units of the Minas Supergroup. Units of the Sabará and Itacolomi groups and of the Espinhaço Supergroup are locally present (Fig. 1).

Banded trondhjemite-tonalite-granodiorite (TTG) gneisses represent the largest proportion of the crystalline basement of the QF, comprising four main litho-structural domes, e. g. Belo Horizonte to the north, Caeté to the northeast, Bação in the central portion and Bonfim to the west. These TTG gneisses are intruded by metatonalites, metandesites, metagranites, pegmatites and Proterozoic mafic dikes (Noce et al., 2007; Farina et al., 2015; Moreira et al., 2016). According to Lana et al. (2013), the magmatic evolution of the TTG crust began as early as 3200 Ma with the emplacement of the 3210 Ma Santa Bárbara Complex, and was affected by three magmatic events at ca. 2930–2900 Ma (Rio das Velhas I event), 2800–2770 Ma (Rio das Velhas II event) and 2750–2700 (Mamona event).

The Rio das Velhas Supergroup (3.0–2.7 Ga; Machado and Carneiro, 1992) is formed by the basal Nova Lima and the upper Maquiné groups (Dorr, 1969). In general, rocks are regionally metamorphosed to the lower greenschist facies (Herz, 1970). The Nova Lima Group is divided into three units (Vieira, 1988, 1991a, b). The lower is composed of komatiitic to tholeiitic basic metavolcanics interlayered with clastic and chemical metasedimentary rocks. The middle unit is composed of mafic and felsic metavolcanics interlayered with carbonaceous metasedimentary rocks, BIFs and felsic metavolcanics. Clastic metasedimentary rocks interlayered with mafic and felsic metavolcaniclastics comprise the upper unit of the Nova Lima Group. These are followed by quartzites and conglomerates of the Maquiné Group.

The Paleoproterozoic Minas Supergroup (2.6–2.1 Ga, Babinski et al., 1995; 2.65 Ga, Cabral et al., 2012) consists of clastic and chemical sedimentary rocks that represent a continental margin sequence. Dorr (1969) subdivided this sequence into the Tamanduá, Caraça, Itabira and Piracicaba Groups. The Sabará and Itacolomi groups respectively represent syn-orogenic flysch and molasse sequences (e.g. Dorr, 1969; Endo et al., 2019a, b), with maximum depositional ages of 2135 \pm 4 Ma for Sabará and 2059 \pm 58 Ma for Itacolomi (Machado et al., 1996). The Espinhaço Supergroup is a metasedimentary sequence deposited between 1.84 and 1.71 Ga (Machado et al., 1989) and covers a small area in the northeast OF.

Baltazar and Zucchetti (2007) and Baltazar and Lobato (2020) proposed four compressional phases (D1 to D4) and one extensional phase (DE) in the QF. The first and second deformation phases (D1 and D2) are related to a progressive deformation event under ductile to ductile—brittle regimes in the Archean. Deformation phase D1 is correlated with N to S tectonic transport, resulting in E-trending reverse faults that dip to the north, sub-horizontal open flexural folds verging to the S, as well as tight to isoclinal folds with axes plunging to ENE. The second phase D2 is

characterized by NW-striking thrust faults in association with tight to isoclinal NW-trending folds, verging SW. Structural features recognized as the D3 phase are NE–SW-oriented, NW-vergent fold-thrust belts in a ductile–brittle regime, with an SE to NW tectonic transport during the Paleoproterozoic Transamazonian orogeny. The extensional structures related to DE phase are associated with the collapse of the Trasamazonian orogen. Furthermore, the fourth deformation phase D4 affects all Proterozoic as well as subjacent units and is correlated to the Brasiliano orogeny in the Neoproterozoic to Early Ordovician (0.65 to 0.45 Ga), in a compressional regime with transport from E to W.

3. Cuiabá gold deposit

3.1. Local stratigraphy

The lithostratigraphy at the deposit area was first defined by Vial (1980) and is described in detail in Vieira (1992), Lobato et al. (2001) and Fernandes et al. (2016). The description that follows is based mostly on these authors.

Cuiabá is dominated by greenschist-facies metavolcanic, metavolcaniclastic and metasedimentary rocks. This succession is related to the lower, middle and upper units of the Nova Lima Group (Vieira, 1988, 1991a, b). For purposes of clarity, the prefix meta will be omitted in this paper.

The lower unit is characterized by a thick (>400 m) succession of fine-grained mafic volcanics composed by chlorite, epidote, quartz, plagioclase and actinolite, interbedded with pelites and lenses of carbonaceous pelites. Mafic volcanics are overlain by the 15-m-thick Cuiabá banded iron formation (Cuiabá BIF), an Algoma-type carbonate-dominated iron formation. Carbonates are the dominant iron-bearing minerals of the Cuiabá BIF, although magnetite- and stilpnomelane-bearing BIFs have been locally described in the mine (e. g., Sena, 2020).

The middle unit is a sequence of alternating carbonaceous pelites, composed of muscovite, quartz, carbonate, chlorite and carbonaceous matter (whole-rock organic carbon content up to $2\,\%$ wt.), and hydrothermally altered mafic volcanic with local intercalations of pelites. The top of the middle unit is comprised of unaltered mafic volcanics with estimated thickness of $150\,\mathrm{m}$.

The >600-m thick upper unit is a sequence of pelites alternating with volcaniclastics of dacitic and rhyolitic composition. Pelites are both micaceous and contain carbonaceous matter, the former with a higher modal composition of carbonate. Mafic dikes up to 30 m wide crosscut all rock types and have similar composition to the mafic volcanics.

3.2. Structural setting

At least three deformational events are related to the structural evolution at the Cuiabá deposit: D1, D2 and D3 (Ribeiro Rodrigues et al., 2007). The first two generations, D1 and D2, are related to a progressive deformation event developed under ductile to ductile–brittle regimes, with fault zones oriented in the NW-SE direction. However, the sense of tectonic transport is object of discussion. Ribeiro-Rodrigues (2007) and Vitorino (2017) considered a frontal ramp from SE to NW, whereas Fernandes (2016) considered a lateral/oblique ramp with NE-SW direction. Generation D1 is marked by tight, reclined folds plunging to ESE with gold hosted by deformed pyrrhotite-rich BIF, whereas D2 show reclined and close folds coaxial to the D1 phase with gold mainly associated with subhedral pyrite in quartz-carbonate veins parallel to fold axial planes (Fernandes et al., 2016; Vitorino et al., 2020).

Orebodies are concordant to D1 linear fabrics, plunging parallel to the intersection lineation and coincident with the Cuiabá fold axis (L₁ = 116/24–35). All lithotypes reveal a pervasive axial planar foliation (Sn = 135/45, Vitorino et al., 2020) that is locally mylonitic, with a prominent mineral lineation (Lmin₁ = 126/22–35) expressed by the preferred orientation of elongated sericite, carbonates and sulfides.

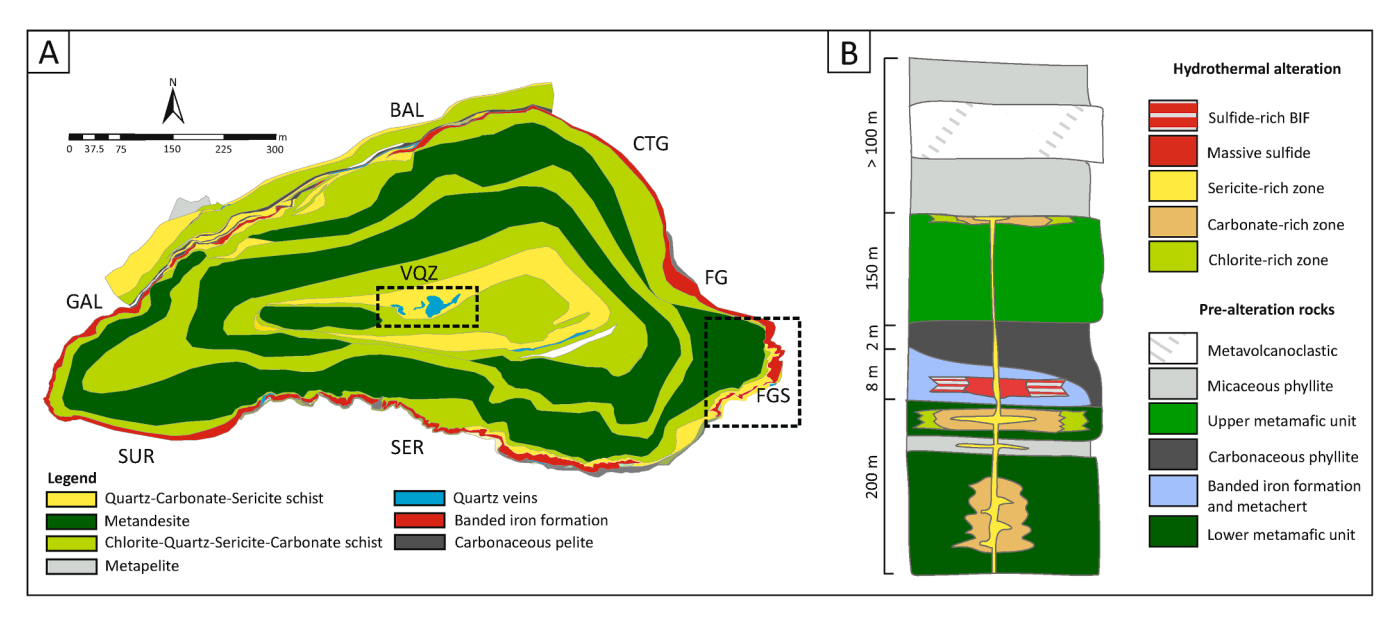


Fig. 2. (A) Geological map of the Cuiabá mine, Level 11 and location of main orebodies omitting upper sedimentary rocks (modified from Vitorino et al., 2020). BAL: Balancão; CTG: Canta Galo; FG: Fonte Grande; FGS: Fonte Grande Sul; SER: Serrotinho; SUR: Surucu; GAL: Galinheiro; DDO: Dom Domingos; GAL FW: Galinheiro Footwall; GAL QTZ: Galinheiro Quartzo; GAL EXT: Galinheiro Extensão; SER FW: Serrotinho Footwall; FGS FW: Fonte Grande Sul Footwall; VQZ: Veio de Quartzo; VIA: Viana. (B) Schematic lithostratigraphic succession at the Cuiabá mine (Fernandes et al., 2016).

Structures recognized as D3 are fault bend folds with sub-horizontal fold axes plunging S and verging W, formed under brittle-ductile conditions by EW-shortening parallel to the foliation S1. These include a crenulation cleavage (S3 = EW-NS/subvertical) and an NS- and EW-trending crenulation lineation, which is parallel to the axes of F3 open folds.

The so-called Cuiabá fold is an overturned anticline with an inverted northern flank and a normal sequence in the southern flank (e.g. Vial, 1980; Ribeiro Rodrigues et al., 2007). This structure is a kilometer-scale, isoclinal fold marked by the contours of the Cuiabá BIF (Fig. 2; Fig. 6 in Ribeiro Rodrigues, 2007). The Cuiabá fold axis plunges 116/35° at the surface and displays a progressive shallowing plunge with depth, with dip angles that vary between 35° at the surface to 12° below level 18 (Vitorino et al., 2020). The genesis of the Cuiabá fold is still being debated (e.g. Vial, 1980; Vieira, 1992; Ribeiro Rodrigues, 1998; Ribeiro Rodrigues et al., 2007; Fernandes et al., 2016).

3.3. Gold mineralization

Several studies have been conducted on the geology and gold mineralization at Cuiabá (e.g. Vial, 1988a; Ribeiro Rodrigues, 1998; Lobato and Vieira, 1998; Costa, 2000; Lobato et al., 2001a, b; Vitorino et al., 2020; Kresse et al., 2018, 2020; Sena, 2020). Gold mineralization is Neoarchean, dated as 2672 \pm 14 Ma by U-Pb SHRIMP monazite (Lobato et al., 2007).

Three main mineralization styles are identified in the Cuiabá deposit: 1) stratabound-replacement in BIF; 2) disseminated, related to hydrothermal alteration in shear zones; and 3) shear-zone-related quartz-carbonate-sulfide veins (Lobato et al., 2001a; Ribeiro Rodrigues et al., 2007). These styles reveal variations in hydrothermal alteration due to variations in fluid-rock interactions (Lobato and Vieira, 1998). Cuiabá orebodies show a strong structural control concordant to the phase D1 linear fabrics, with a consistent down-plunge continuity dipping SE, parallel to the intersection lineation L_1 (Ribeiro Rodrigues et al., 2007).

Archean gold mineralization in the QF province has been classified in three types based on the ore-associated minerals and related structures (Vieira and Oliveira, 1988): (i) Type-1, stratabound-replacement style hosted in BIF and *lapa seca*, a range of carbonate-rich hydrothermal-alteration rock products containing quartz, albite, and subordinate

muscovite (Lobato et al., 2001b; Vial et al., 2007). This type is controlled by D1 shear zones and associated folds in which pyrrhotite is dominant, with minor pyrite and arsenopyrite. (ii) Type-2, replacement style in FFB and *lapa seca*, migrating from D2 fractures and shear zones that cross-cut D1 host rock structures, in which pyrite, arsenical pyrite and arsenopyrite are typical. (iii) Type-3, a quartz-sulfide vein style in a variety of host sedimentary and volcanic rocks, typically pyrite-rich, with scattered subordinate pyrrhotite along D1 and D2 shear zones. The Cuiabá gold ore is type-2 dominated, although types-1 and -3 occur subordinately (Vieira et al., 1991).

The six main ore shoots are contained within the Cuiabá BIF horizon and grade laterally into non-economic mineralized or barren BIF: Fonte Grande Sul, Canta Galo, Balancão, Galinheiro, Galinheiro Extensão and Serrotinho orebodies. The typical sulfide assemblage of the Cuiabá BIF is pyrite-pyrrhotite-arsenopyrite, with minor chalcopyrite and sphalerite. Gold is mainly included in pyrite, pyrrhotite and arsenopyrite, varying in size between 10 and 80 μm , and may occur as free particles along crystal boundaries or filling fractures in pyrite, as well as free particles in the quartz-carbonate matrix (Ribeiro Rodrigues et al., 2007).

The Fonte Grande Sul (FGS) orebody contains the largest Cuiabá ore resources, 1.98 Moz at an average grade of 7.68 g/t Au (Resources and Reserves Evaluation Report, AngloGold Ashanti, 2019). The orebody is situated in the SE closure of the Cuiabá fold and increases in area progressively with depth in a constant thickness of 4 to 6 m. The mineralized BIF consists of rhythmic alternation of dark, white, and ochercolored, millimeter- to centimeter-thick bands, intensively sulfidized, rich in carbonaceous material, fine-grained quartz and carbonates (Ribeiro Rodrigues et al., 1996a, 2007). Associated country rocks show strong sericite, carbonate and chlorite alteration (e.g., Kresse et al., 2018).

Mafic volcanic-hosted orebodies associated with the upper mafic volcanic unit were locally mined in the past, e.g. Viana and Galinheiro Footwall orebodies. Three occurrences were recently discovered in quartz-carbonate veins hosted in the lower mafic volcanic unit: Veio de Quartzo, Fonte Grande Sul Footwall and Serrotinho Footwall. Vitorino et al. (2020) classify these into four different vein systems according to mineralogical and structural features: V1, V2, V3 and V4, associated with hydrothermal alteration and ductile–brittle shear zones. The same authors indicate that gold varies in size between 1 and 250 μm , is mainly

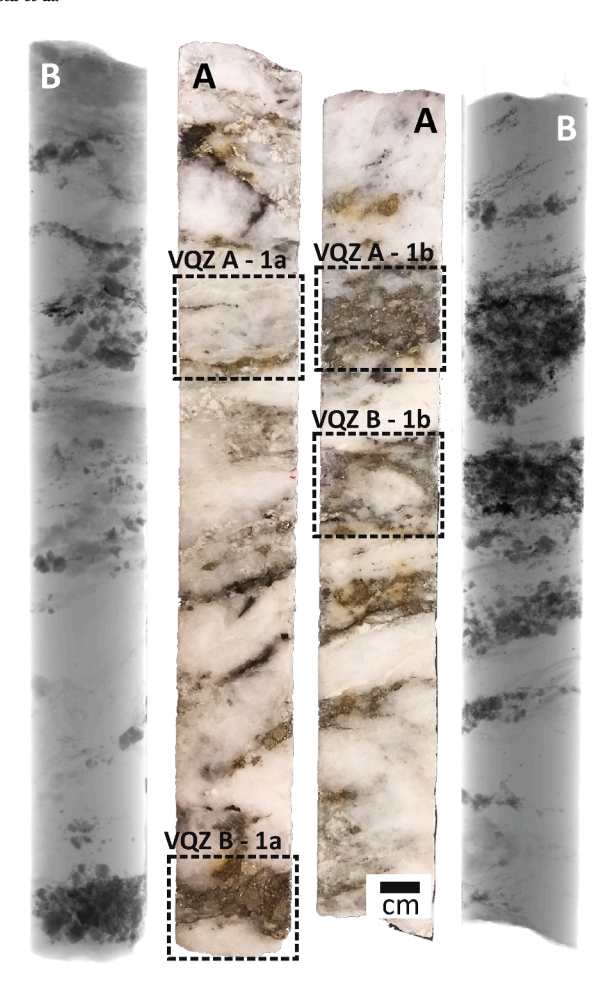




Fig. 3. A) Core sample VQZ1 of the Cuiabá vein-style ore, Veio de Quartzo Orebody, showing the HRXCT studies zones. The sample is from a 1.11 m interval with average assay values of 193.46 g/t Au. B) Brightness manipulated digital radiographs from VQZ1. Highly mineralized zones appear as massive dark aggregates of higher net X-ray attenuation, suggesting regions to be scanned by computed tomography. C) Replacement-style BIF sample from Fonte Grande Sul orebody level 19, 1st left sublevel. A physical marker was attached to the surface of FGS-1A sample at the same orientation of the intersection lineation L1 (106/25) measured on site; subsample FGS-1B is indicated by dashed box.

free within quartz-carbonate veins, but also disseminated in sulfide minerals in the host rock.

Located in the center of the Cuiabá fold, the Veio de Quartzo (VQZ) orebody is associated with a N70 $^{\circ}$ E shear zone, dipping parallel to the main orebody plunge (116/15 $^{\circ}$). Surface and underground drilling data show that the shoot has a continuous mineralized zone up to 2 km in depth along the plunge and may achieve up to 30 m in thickness. Average grades are around 5 g/t, locally reaching up to 500 g/t due to nugget effect (Vitorino et al., 2020).

4. Materials and methods

4.1. Sample description

4.1.1. Drill core VQZ orebody - VQZ1

We selected the drill core VQZBUD0063 from the Veio de Quartzo-VQZ Orebody (Fig. 3A) of approximately 3 cm in diameter and 51 cm long, with an average grade of 193.46 g/t Au in a 1.11 m interval. The ore sample corresponds to the V1 vein system, of which the longest axis of V1 veins coincides with the Lmin1 (Vitorino et al., 2020). Four 3-cm core segments were selected to be scanned in pairs (VQZ1 A-1a; VQZ1 A-1b; VQZ1 B-1a; VQZ1 B-1b).

The ore sample consists of a smoky and white quartz-carbonate matrix containing sulfide-rich portions, mostly pyrite and minor pyrrhotite, chalcopyrite, sphalerite and galena. Milky quartz veinlets and millimetric sericite and chlorite-rich films or pods are present, as well as

sparse millimetric rock fragments, possibly from mafic host rock. Gold size distribution is heterogeneous, and particles can be free in the matrix, mainly located along the boundaries of pyrite, pyrrhotite, galena, sphalerite and chalcopyrite, or enclosed in pyrite (Fig. 4A, B, C).

4.1.2. BIF sample, FGS orebody - FGS-1

The selected BIF-ore sample from the Fonte Grande Sul orebody level 19, 1st left sublevel, is approximately $5\times5\times9$ cm in size (FGS-1A, Fig. 3C). A sub-sample FGS-1B adjacent to -1A, of $1\times1\times3$ cm, was also investigated. The BIF consists of rhythmic alternation of dark and ocher-colored iron carbonates and smoky and white quartz bands, with intensively sulfidized bands containing pyrrhotite and arsenopyrite, and minor pyrite. Arsenopyrite is acicular to platy, rather than rhombic, and may overgrow pyrrhotite. Gold occurs as free particles along crystal boundaries or filling fractures in pyrrhotite, pyrite or arsenopyrite, as well as free particles in the quartz-carbonate bands. A physical marker was attached to the surface of FGS-1 sample at the same orientation of the intersection lineation L_1 (106/25) measured on site.

4.2. Digital radiographs

Digital radiography (DR) has been applied as a means of identifying samples with a greater probability of containing gold particles for more detailed HRXCT analysis (Kyle et al., 2008). Vein-style mineralization typically has an erratic concentration of gold particles; thus DR was used to evaluate portions for scanning the VQZ1 sample. Digital radiographs

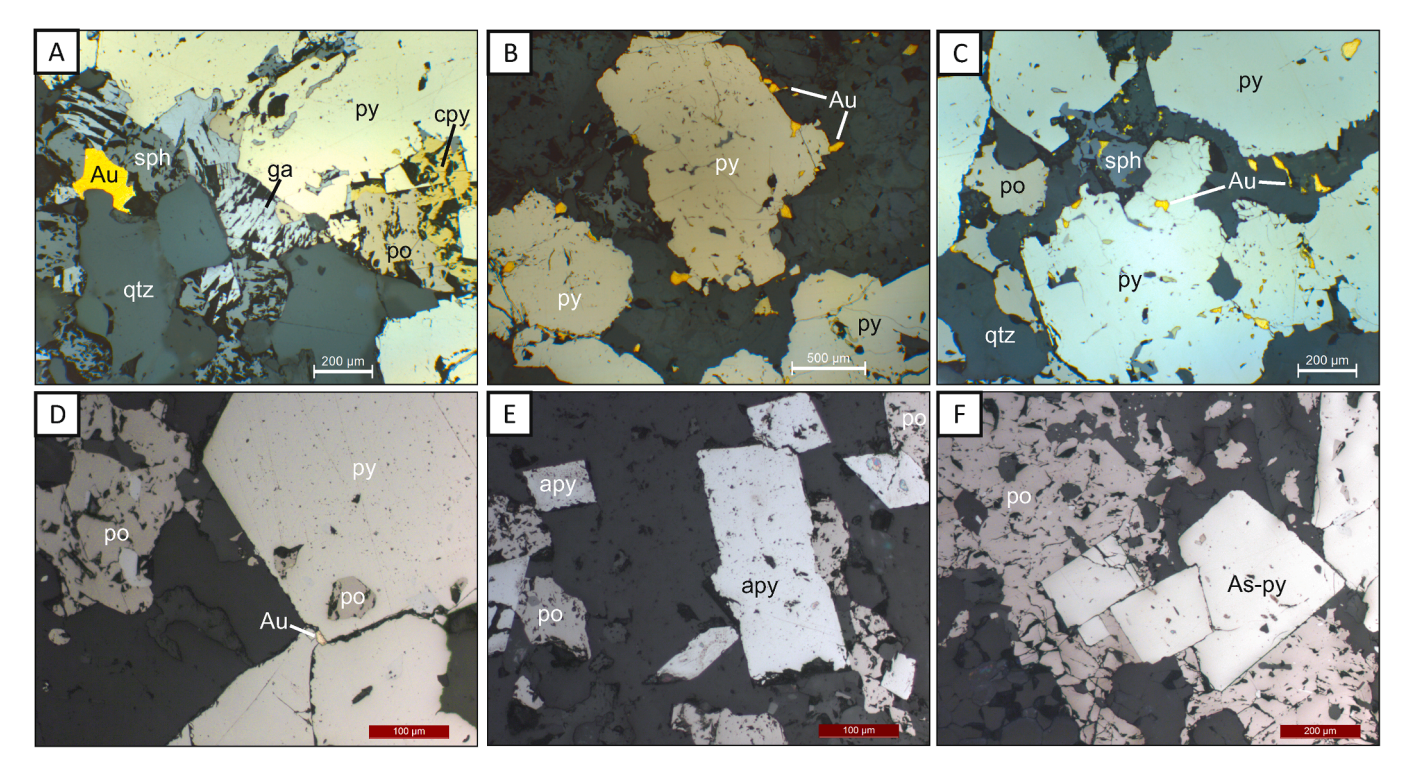


Fig. 4. Photomicrographs taken under reflected light and uncrossed nicols. A, B, C) VQZ1 sample consists of a smoky and white quartz-carbonate matrix with mostly pyrite and minor pyrrhotite, chalcopyrite, sphalerite and galena. Gold size distribution is heterogeneous and is mainly located at sulfide grain boundaries, enclosed in pyrite, or as free particles in the matrix. D, E, F) FGS-1A sample consists of iron carbonates and smoky and white quartz containing pyrrhotite, and minor pyrite and arsenopyrite. Gold occurs as filling fractures or enclosed in pyrrhotite or pyrite, as well as free particles. Arsenopyrite locally overgrows pyrrhotite (F). qtz: quartz; ga: galena; apy: arsenopyrite; py: pyrite; As-py: arsenic pyrite; po: pyrrhotite; sph: sphalerite; cpy: chalcopyrite; Au: gold.

Table 1 Scan parameters.

Sample	Inst. ^a	Scan ^b	kV	mA	Filter	внс с	Voxel size (µm)	NS ^d	r _{PSF} (pix)	r _{PSF} (μm)	CT_{th}	CT_{Au}
VQZ1 A	NSI	nc	220	0.26	Brass	0.200	18.8	1670	4.45 ± 0.88	84	31,000	62,439
VQZ1 B	NSI	nc	220	0.26	Brass	0.200	18.8	1739	5.32 ± 1.01	100	32,000	65,462
FGS - 1A	NSI	hc	220	0.25	Brass	0.325	40.2	2342	6.32 ± 0.72	243	4051	38,379
FGS - 1B	NSI	hc	140	0.22	Al foil	0.150	9.74	3223	5.94 ± 2.68	58	14,336	65,024

^a Instrument: NSI scanner, ^b Scan mode: non-continuous, nc; helical continuous, hc, ^c Beam-hardening correction, ^d number of slices,

are obtained by X-ray imaging an object from a single side, and the attenuation of the X-ray beam passing through the object is represented in ranges of grayscale values. These images are typically displayed using the opposite convention as CT images, in which higher attenuation values correspond to darker grayscale values. Because of its extreme density, gold has the highest attenuation and thus the lowest grayscale values. On the other hand, rock-forming minerals in the matrix appear in general brighter than other phases, with metallic minerals being dimmer.

Image brightness and contrast were manipulated in the open source image processing program ImageJ (imagej.nih.gov/ij) to aid phase differentiation. Isolated and large gold particles are easily identified in the quartz-carbonate matrix (Fig. 3B). However, in the sulfide-rich portions, associated fine and numerous gold particles are not clearly distinguished. These highly mineralized zones appear as massive aggregates of higher net X-ray attenuation, suggesting portions to be imaged by computed tomography.

4.3. High resolution X-ray computed tomography

Selected samples were scanned at The University of Texas High-Resolution X-ray CT Facility under a range of conditions (Table 1). The facility, and the meaning of various scanning parameters, is

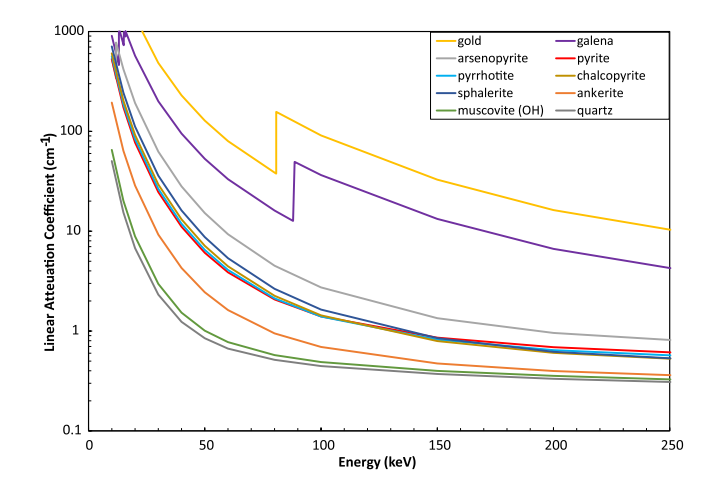


Fig. 5. Linear attenuation coefficients as a function of X-ray energy for common Cuiabá minerals. These curves allow prediction of the grayscale contrast between each mineral in HRXCT images. The values shown here are based on end-member compositions and densities and were calculated using the MuCalc (Hanna and Ketcham, 2017).

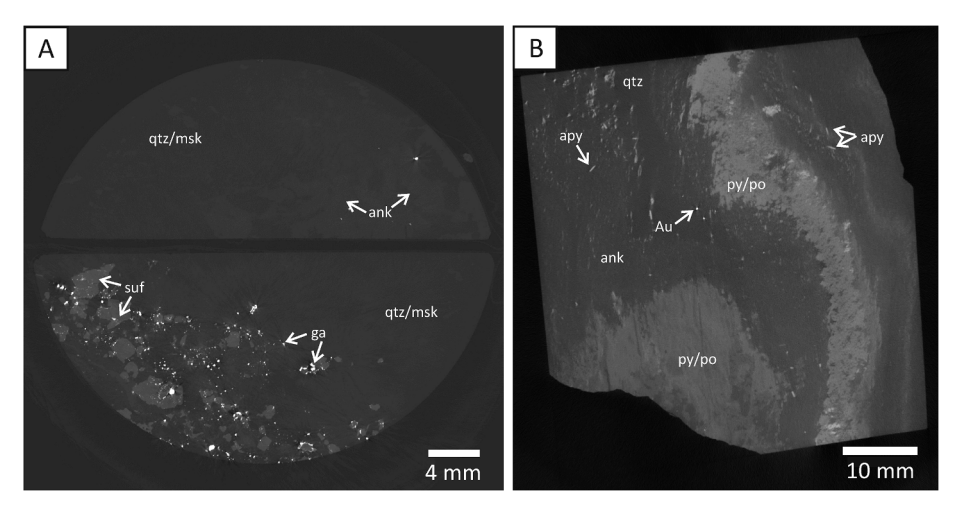


Fig. 6. Representative HRXCT slices of A) VQZ1 A and B) FGS-1A showing grayscale contrast between mineral phases. Gold particles have the higher grayscale values and thus are brighter; rock-forming matrix has the lowest grayscale values and sulfides have intermediate values. qtz: quartz; msk: muscovite; suf: sulfides; ga: galena; ank: ankerite; apy: arsenpyrite; py: pyrite; po: pyrrhotite.

described in detail by Ketcham and Carlson (2001), as well as the UTCT website www.ctlab.geo.utexas.edu.

The reconstructed data volumes were analyzed using Avizo (www. fei.com/software/avizo-3d-for-materials-science/), ImageJ (www. imagej.nih.gov/ij), and Blob3D (Ketcham 2005).

4.4. Phase differentiation

The X-ray attenuation in a CT scan is represented in ranges of grayscale values, in which a unique value is attributed to a voxel. The grayscale value associated with each mineral phase can be evaluated by plotting the linear attenuation coefficients of the different materials over the range of the available X-ray spectrum and comparing their attenuation at the X-ray energy applied during the scan.

Linear attenuation coefficients were calculated for the typical mineral association of the Cuiabá BIF- and vein-hosted ore (Fig. 5). At the scan energy of 220 keV and 140 keV, gold is not only distinguished from the typical rock-forming matrix, e. g., quartz and ankerite, but also from the major metallic sulfides, arsenopyrite, pyrite, pyrrhotite, and sphalerite. The attenuation coefficient spectra for these sulfide minerals are similar because of similar mass densities, making these minerals more difficult to differentiate from one another. Due to its elevated density and lead content, galena has a higher linear attenuation, intermediate between the other sulfides and gold.

In CT images, these distinctions of linear attenuation coefficients define the grayscale contrast between each mineral identified. Gold has the highest attenuation and thus the highest grayscale values, the opposite convention applied to digital radiographs. Rock-forming minerals (quartz and iron-carbonates) appear darker than other phases and sulfide minerals have intermediate values (Fig. 6).

4.5. Data processing

Quantitative measurements of gold particles are particularly challenging due to the finite resolution of CT data, because most particles are small relative to the sample size. As a result, small gold particles appear dimmer than large ones. Measurements that account for this effect are based on establishing the X-ray attenuation signal associated with a particle and converting that to a volume, which requires a calibration that relates how much volume corresponds to a given X-ray attenuation in a finite number of voxels. However, the value depends not only on the X-ray source energy but also on how the bulk sample affects the spectrum, which is a function of its size, density and atomic number variation among rock constituents.

Each voxel in the scan data effectively represents a volume of the rock, so if more than one mineral occupies this voxel volume, the CT value represents a weighted average of the X-ray linear attenuation coefficients of both minerals. Referred as partial volume effects (PVE), these artifacts must be considered when quantifying accurate particle volume. The CT values are also affected by larger-scale blurring that can be characterized by a point spread-function (PSF), the effect of which is to distribute some of the signal from a single voxel among neighboring ones (Ketcham and Mote, 2019). The combination of partial-volume and blurring effects is referred to as the PVB effect (Ketcham and Mote, 2019). In the present study, these artifacts were compensated by the PVB method proposed by Ketcham and Mote (2019), in which features are segmented to encompass their total attenuation signal that is then converted to a corrected volume.

The PVB method is a formalization and expansion of methods used in previous studies for this purpose (e.g., Mote et al., 2005; Kyle and Ketcham, 2015), including techniques for calibration and improved shape and orientation measurement. Using a fabricated rock consisting of gold grains suspended in quartz and epoxy, Ketcham and Mote (2019) demonstrated that grains volumes can be reliably measured even when they are heavily blurred (less than 1.5 voxels in true radius), and proposed resolution guidelines to ascertain when shape and orientation data are reliable. The present study is the first application of the PVB method to a natural specimen. Data were processed in the Blob3D software, a program designed to define, separate and analyze objects in three-dimensional data sets developed at the University of Texas at Austin (Ketcham, 2005).

4.5.1. PSF size

The procedure for measuring the point spread-function consists of drawing a series of linear traverses in the data, normal to sharp interfaces between two materials, allowing the software to quantify the amount of blurring along a set of nine parallel lines surrounding each traverse (Ketcham and Hildebrandt, 2014). Six separate traverses were averaged to determine the scan characteristic PSF parameter (r_{PSF}) using only measurements for which the uncertainty in the mean r_{PSF} was below 1.0 voxel. The obtained functions for each data set are presented on Table 1. Generally, 95% of the attenuation signal from material within a voxel lies within a spherical region of diameter r_{PSF} .

4.5.2. Segmentation

The segmentation process normally consists of attributing a range of grayscale values to a given phase of interest. In an ideal case, the histogram of CT values has a deep and sharp valley between two different

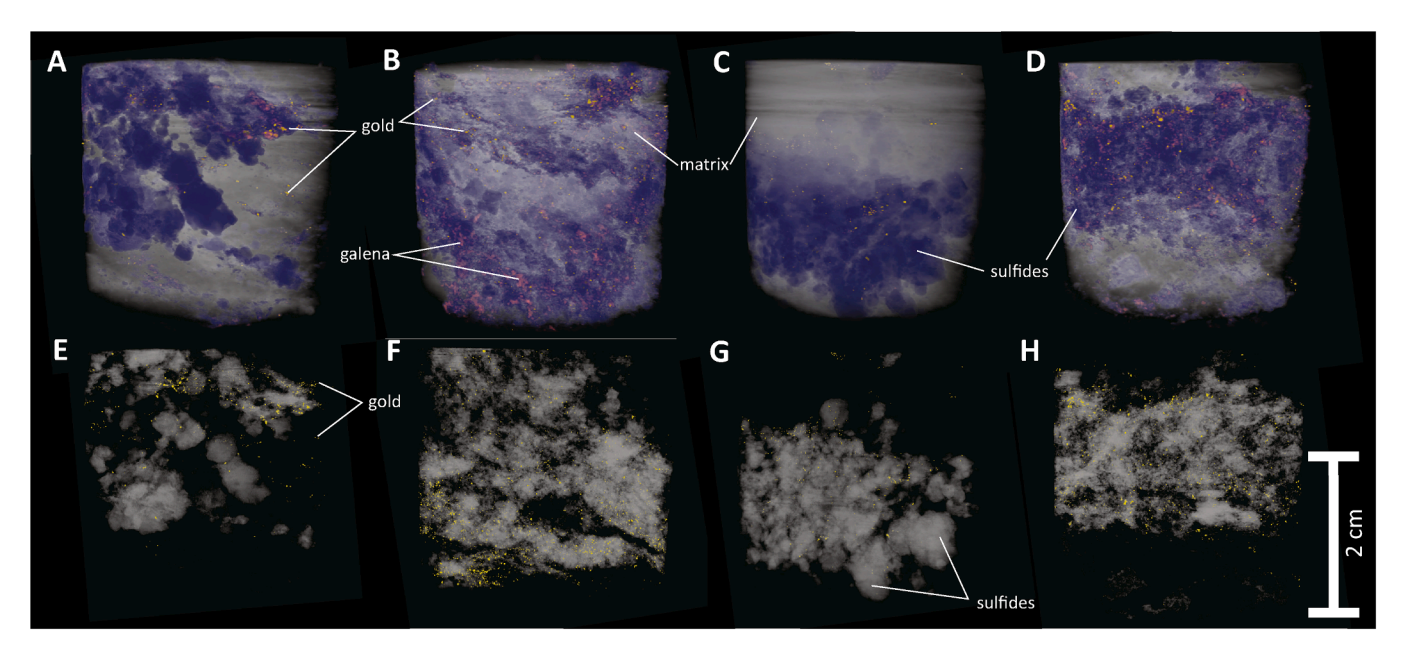


Fig. 7. Three-dimensional (3-D) volume renderings of X-ray CT data of sample VQZ1. Sulfide minerals assigned in purple; galena in pink; matrix in white; gold in yellow, for sections A) VQZ1 A-1a, B) VQZ1 A-1b, C) VQZ1 B-1a, D) VQZ1 B-1B. Sulfide minerals in white; matrix transparent; gold in yellow, for sections E) VQZ1 A-1a, F) VQZ1 A-1b, G) VQZ1 B-1a, H) VQZ1 B-1B. (For interpretation of the references to color in this figure legend, the reader is referred to the web version of this article.)

minerals, and thus a threshold value is established as the midpoint value between these two phases. However, there is no single threshold value that allows accurate volume measurement if particle sizes approach the PSF. Thus, the most accurate measurements for each particle are obtained using the PVB method. The PVB method interprets each voxel associated with a particle as having a partial signal from the phase of interest, but also affected by blurring from surrounding material. By combining the voxels associated with a single particle and extracting the portion of signal from that particle, accurate volumes, shapes, and orientations can be obtained that are resistant to the effects of limited spatial resolution.

Segmentation for PVB processing consists of selecting the entire set of voxels influenced by each particle, which due to blurring is inevitably larger than the particle itself. First, the data are processed using standard thresholding using a value that successfully selects the particles of interest and leaves out other material. Selected threshold values (CT_{th}) are shown in Table 1. Using the Blob3D "Segment" module, each selected area, or "blob", is then dilated by an additional 1 to 3 voxels in 3D, depending on the degree of blurring (i.e. r_{PSF}) and the amount of material captured in the initial threshold, until its entire attenuation anomaly is encompassed.

4.5.3. Volume measurements

Volume measurements are obtained by converting the entire CT signal associated with the mineral particle of interest to a PVB-corrected volume, using a simple linear function that relates the CT number of each voxel i encompassed by the particle (CT_i) with the ideal or endmember CT numbers of the phase of interest (CT_{Au}) and the CT numbers of the surrounding matrix adjacent to the voxels of interest (CT_{mat}) :

$$v_{PVB} = v_{voxel} \sum_{i} \frac{(CT_i - CT_{mat})}{(CT_{Au} - CT_{mat})}$$

where v_{voxel} is the constant volume of a single data voxel.

The CT_{Au} is estimated as the maximum CT number observed for gold across the entire scanned volume, for which the brightest particles with a short axis larger than $2x \, r_{PSF}$ (Ketcham and Mote, 2019) should have a central region that is not blurred (Table 1). For FGS-1A and 1B, the CT_{Au}

was defined by the maximum CT numbers gold particles that came close to this criterion, but may have been slightly too small, which would result in a slight overestimate of gold volumes.

In the case of VQZ1 sample the segmented particles were not large enough to precisely determine CT_{Aus} , thus the value was defined as the maximum CT number of the largest particle with all three axes larger than r_{PSF} . This procedure may result in a slight over-estimation of particle volumes, which would result in the actual gold particles being smaller than the measurements by a uniform factor.

Because the sample matrix is heterogeneous, and thus has a wide range of CT values, local CT_{mat} is computed for each particle by averaging the CT values in a one-voxel-thick annular shell immediately beyond the selected area.

4.5.4. Shape measurements

Once the selected region during segmentation is expanded, and is larger than the actual particle, the number of voxels (N_f) truly encompassed by the gold particle must be calculated based on the corrected volume and the voxel volume:

$$N_f = \frac{v_{PVB}}{v_{voxel}}$$

An isosurface is fitted to the N_f voxels with the highest CT numbers and then used to calculate a best-fit ellipsoid, sphericity and caliper parameters. Sphericity is calculated as the ratio of the surface area of the equivalent-volume sphere to that of the isosurface surrounding the N_f voxels. The caliper dimensions are defined by the minimum bounding box that fits the particle: BoxC, BoxB and BoxA are the respective dimensions of the shortest caliper length, the shortest caliper length orthogonal to it and then the caliper length orthogonal to the first two (Blott and Pye, 2008).

Quantifying the PSF of the CT data also allows us to define when shape measurements are in danger of being affected by resolution limitations. Ketcham and Mote (2019) advise that shape determinations are reliable if both BoxC and the difference between BoxB and BoxC both exceed r_{PSF} . Points that do not pass these criteria are plotted in gray in the diagrams below.

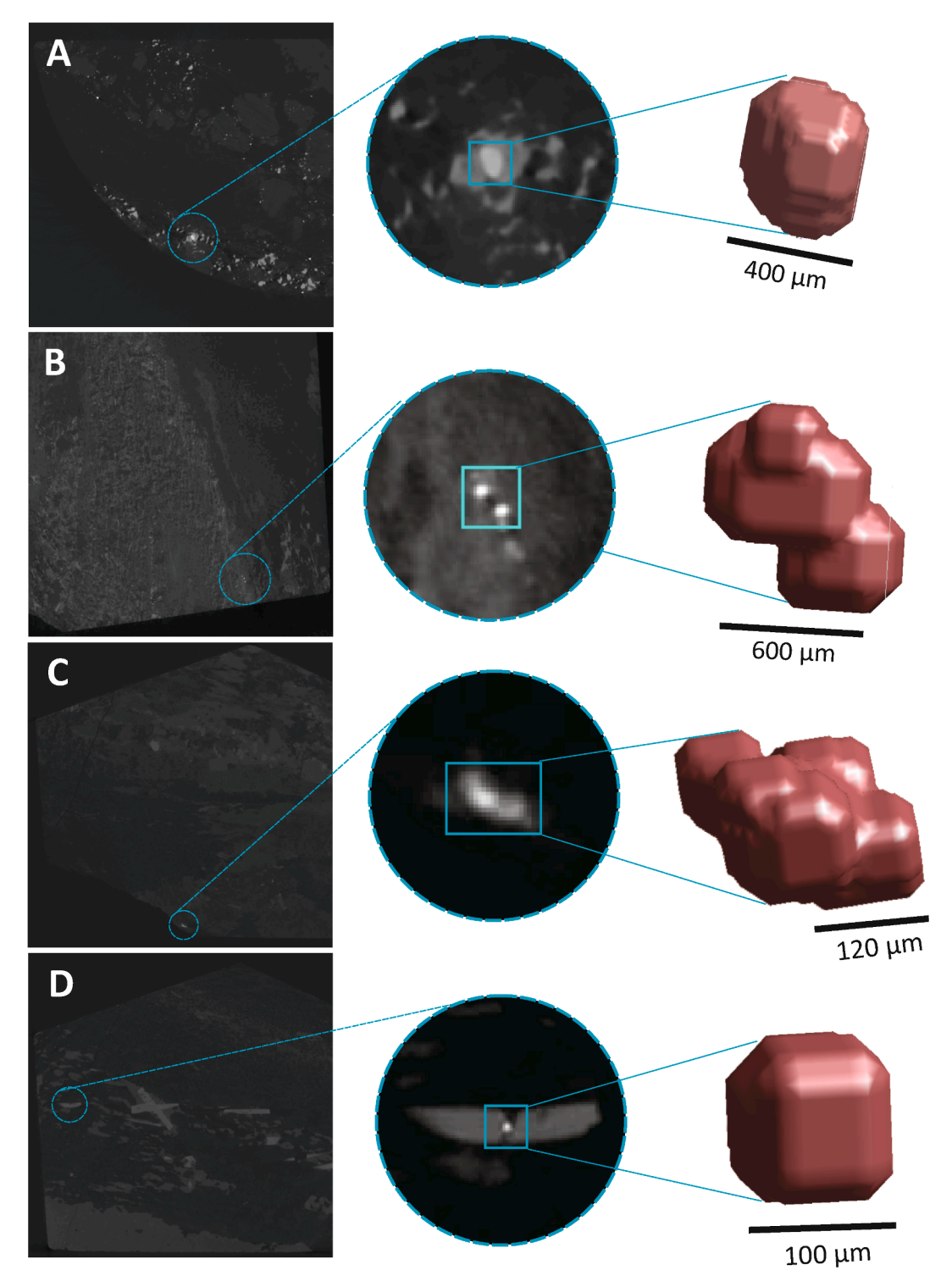


Fig. 8. Examples of grayscale HRXCT slices showing the segmented and extracted gold particle. A) VQZ1: Gold particle enclosed in galena; B) FGS-1A: Gold enclosed in pyrite or pyrrhotite; C) FGS-1B: free gold particle; D) FGS-1B: Gold filling arsenopyrite fracture.

4.5.5. Structural measurements

Extracting structural data from a CT dataset require that the scanned sample is oriented in space. Before scanning, a physical marker was attached to the surface of sample FGS-1A at the same orientation of the intersection lineation L_1 (106/25) measured on site. The lineation direction is faithfully recovered, but there is an unknown rotation around that vector because the orientation was not preserved during sampling. During data processing we defined a coordinate system using the Blob3D "Extract" tool that captures the lineation direction, but suffers from the

unknown rotation around this vector, to determine if gold particles are oriented along a preferential direction. Each segmented particle is fitted to an ellipsoid, and the three axes are rotated into the defined coordinate system.

As with shape measurements, the reliability of orientation determinations can be impacted by resolution effects. Ketcham and Mote (2019) found that maximum and/or minimum axis orientations are optimally repeatable when their respective lengths differ from the intermediate axis length by a factor of \sim 2; the closer these axes are to the

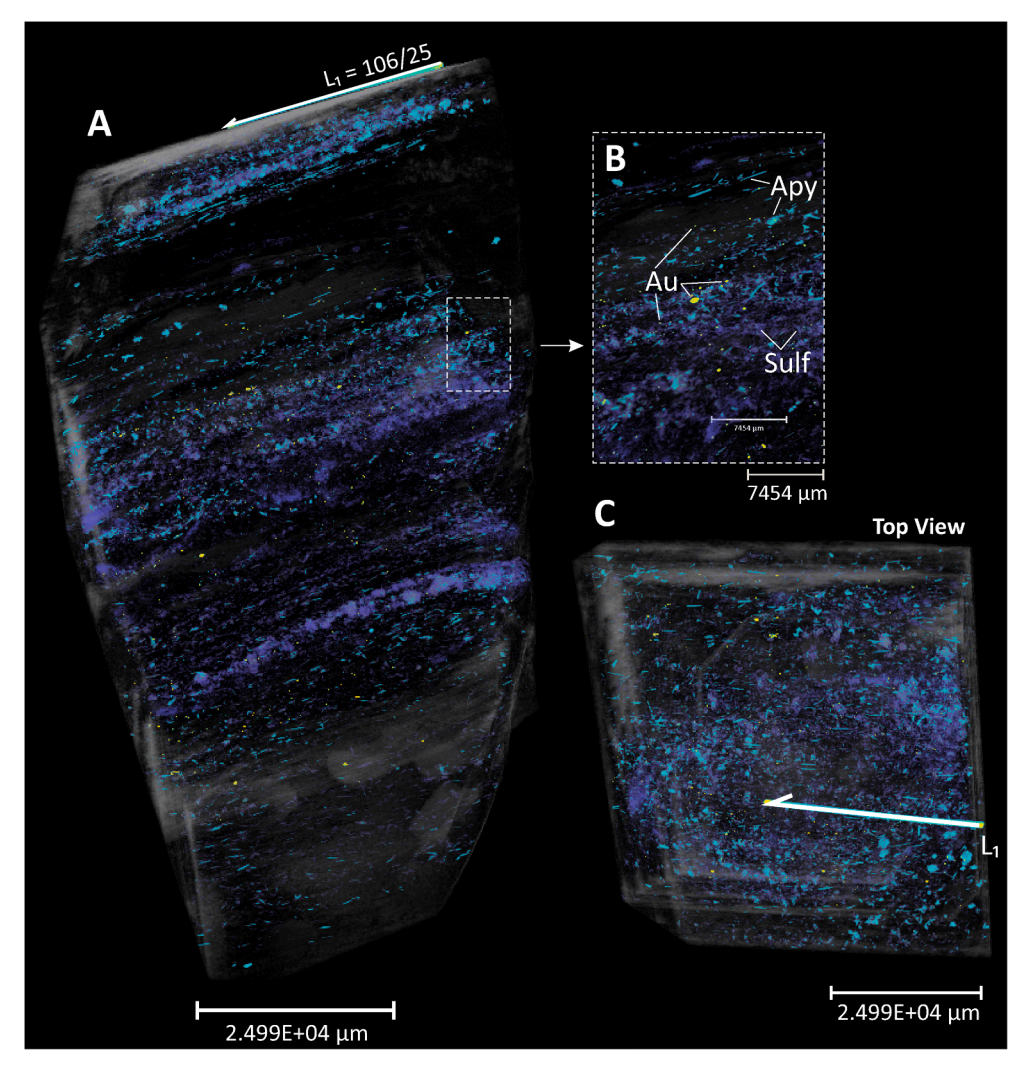


Fig. 9. 3-D volume rendering of sample FGS-1A. Sulfide minerals assigned in purple; arsenopyrite in blue; matrix transparent; gold in yellow. A) Side view; B) Close-up of sulfide-associated gold particles; C) Top view. (For interpretation of the references to color in this figure legend, the reader is referred to the web version of this article.)

intermediate, the more noisy their orientations become. As before, grains that meet this criterion are plotted in color, and those that do not are plotted in gray.

5. Results

5.1. Gold characterization

The 3-D rendered sections from the vein-hosted ore sample VQZ1 show that gold particles are mainly free in the quartz-carbonate matrix, although many particles are in direct contact with sulfide minerals (Fig. 7; Video 1) and also enclosed in them (e.g. galena, Fig. 8A). Pyrite, chalcopyrite, sphalerite, galena and pyrrhotite are indicated as the same phase due to close linear attenuation coefficients in this X-ray CT study. Sulfide crystals are sub-euhedral to euhedral, slightly oriented, and unevenly distributed throughout the scanned core sample (Fig. 7); galena-rich sections display a higher number of gold particles (Fig. 7C, D, G, H; Video 2).

Three-dimensional images from the BIF-hosted ore sample FGS-1 reveal that gold particles form bands (Fig. 9A, C; Video 3) in association with high sulfide zones in iron carbonate-rich bands (Fig. 10A, B; Video 4). Pyrite and pyrrhotite are assigned as the same phase due to scan limitations, but ore petrography revealed that pyrrhotite is the dominant iron sulfide. Gold particles are enclosed in arsenopyrite

(Fig. 10D), filling fine fractures (Fig. 10F, Fig. 8D) or enclosed in massive pyrrhotite or pyrite (Fig. 10G, Fig. 8B), and occur as well free in quartz veins in BIF (Fig. 8C, 10E).

A summary of measurements of gold particles at the Cuiabá deposit regarding size and volume is provided in Table 2; shape statistics are shown in Table 3. Because the segmented gold particles are not large enough to accurately define the end-member CT number for gold (CT_{Au}) in the vein-hosted VQZ1 sample, the identified gold particles are smaller than the indicated measurements by a uniform factor.

In the CT data of the VQZ1 core sections, 15,231 gold particles are identified. Particle volumes span from 8.31E to 07 to 2.77E-02 mm³ and the long axes of measured particles range from 56 μm to 1.4 mm, with most from 50 to 150 μm (Fig. 11A). Short axes range from 37 to 418 μm , with most between less than 50 to 100 μm long (Fig. 11B). However, as the minimum size that can be detected and its shape accurately quantified is a function of the CT resolution, the smaller measured axes may not represent the dimension of the finest particles.

The CT data point-spread function (r_{PSF}), which defines true resolution, has a size of respectively 100 and 105 µm for scans VQZ1 A and VQZ1 B. Thus, particles with dimensions approaching this limit have axis and shape measurements affected by blurring. The criterion used in the present study indicates particles for which shape measurements are most accurate where the short axis, or the difference between the intermediate and the short axis, is larger than the absolute r_{PSF} value;

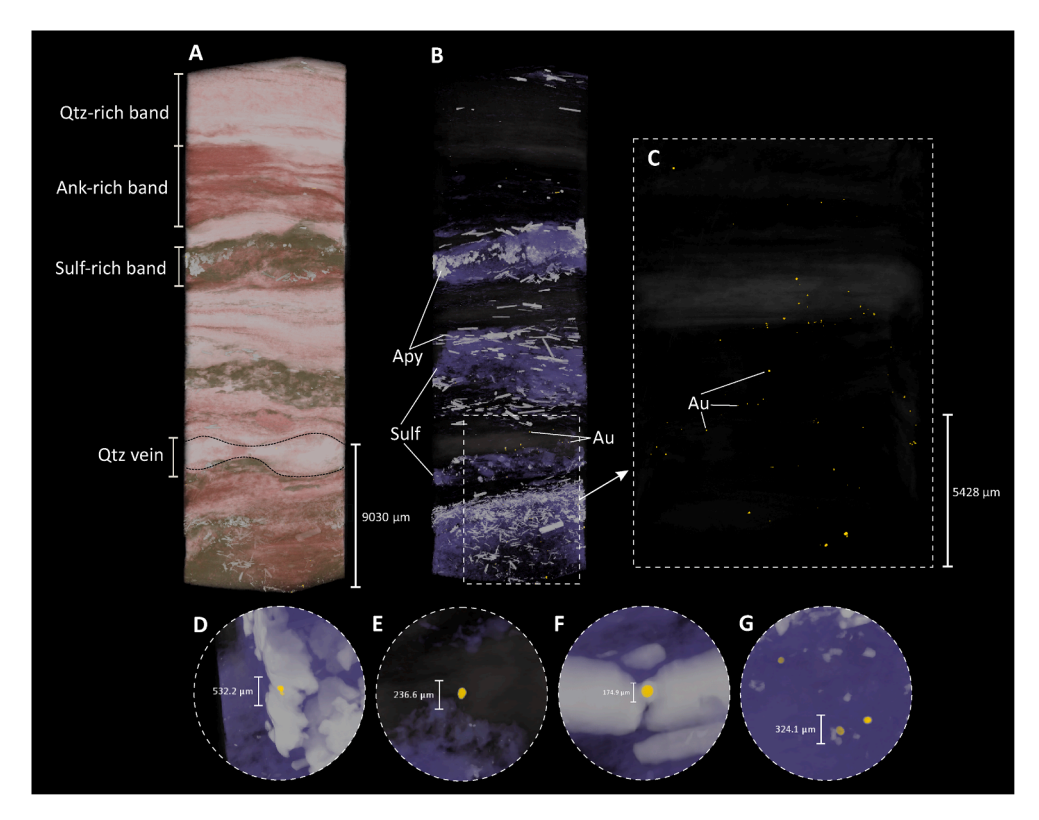


Fig. 10. 3-D volume rendering of sample FGS-1B. A) Banded iron formation rendering. B) Sulfide minerals assigned in purple; arsenopyrite in gray; matrix transparent; gold in yellow. C) Sulfide minerals and matrix transparent; gold in yellow. D) Gold enclosed in arsenopyrite. E) Free gold. F) Gold filling arsenopyrite fracture. G) Gold enclosed in sulfides. (For interpretation of the references to color in this figure legend, the reader is referred to the web version of this article.)

particles not meeting these criteria appear more equidimensional than they really are.

The data are plotted on Blott and Pye (2008) diagrams, utilized to classify particle shapes. Gold particles above the r_{PSF} limit are dominantly sub-equant to prolate spheroid, and the minority is roller or oblate spheroid, whereas particles below this limit appear to be more sub-equant to equant spheroid (Fig. 12A, B, C, D). Sphericity parameters support shape results, in which equant particles approach 1.0 and particles with distinct axes length deviate from 1.0 (Table 2).

A total of 663 gold particles have been measured in the FGS – 1A, and 124 in subsample FGS – 1B (BIF). In FGS – 1A, gold volumes range from 1.46E to 04 to 2.98E-02 mm³. Long axes range from 71 μm to 1.298 mm and short axes from 46 to 328 μm ; most particles have long axes ranging from 100 to 150 μm (Fig. 11C) and short axes between 75 and 125 μm (Fig. 11D). The CT data point-spread function, r_{PSF} , is 243 μm for scan FGS – 1A, revealing that most particles are below the r_{PSF} limit and are mainly sub-equant to equant spheroids, though some particles have prolate and roller shapes (Fig. 12E).

The FGS – 1B sample data show particle volumes ranging from 4.35E to 06 and 3.21E-04 mm³. Long axes span from 23 to 268 μm , and of these most are dominantly from 50 to 150 μm (Fig. 11C); the short axis ranges from 18 to 79 μm , mainly between 18 and 50 μm (Fig. 11D). Gold particles are mainly below the r_{PSF} limit, revealing a dominant equant to sub-equant shape except a few prolate-spheroid- and roller-shaped particles (Fig. 12F). The differences in size and volume distributions between samples FGS-1A and -1B are expected, because the FGS-1B data were obtained at higher resolution and thus able to reveal finer particles.

5.2. Structural analysis

Results from the BIF sample FGS-1A show that acicular arsenopyrite are highly aligned with the indicated mineral and intersection lineation

L1 and are strongly associated with gold-rich portions (Fig. 9B; Video 4).

The bubble charts of long (Fig. 13A) and short axis orientation (Fig. 13B), with bubble sizes regarding particle volumes on equal-angle upper hemisphere projections, reveal that larger particles display consistent clustering, whereas finer particles are dispersed. Considering the resolution of the scans and associated PVB effect, finer particles tend to appear equant to sub-equant and the resulting orientation data are much noisier.

Major and minor axis distributions were further analyzed on equalarea lower hemisphere projections (OpenStereo, 2010). As mentioned previously, long axis orientations are more reliable if they are twice as long as the intermediate axis, and short axis orientations are more reliable if they are half the intermediate axis length. This criterion is met in the FGS-1A scan for the long axis of 28 particles and for the short axis of 1 particle out of a total of 663 segmented particles, indicating that the measurements are mostly noisy in this dataset, but still able to form a recognizable pattern that can be linked to the regional structure.

Considering all particles, the long axis orientations establish a uniaxial girdle (Fig. 14A). The obtained measurements are not fully oriented according to true geological coordinates, but this preferential alignment indicates that grains are indeed oriented along a plane that contains the intersection lineation L_1 . A slight concentration observed from contours in the northwest sector is likely a result of several small particles with the exact same orientation overlapped, reflecting the tendency of these particles to be along the orthogonal voxel grid in the scans. Thus, they do not show a true orientation with regards to the sample. The overall fabric is planar, as defined by the great circle, despite the particles being more elongated than flattened. The short axis orientations display a maximum density at the pole of the long axis girdle and scattered points, again justified by the noisy orientations of particles whose short axes are not strongly different from their intermediate ones (Fig. 14B).

Table 2Gold particles measurements from the Cuiabá deposit samples.

Sample	Measured gold particles		Long Axis Length (µm)	Short Axis Length (µm)	Volume (mm³)	Sphericity
VQZ A	1271	Min	65	47	1.20E-	0.4590
– 1a		Max	1077	368	04 2.06E- 02	0.9732
		Mean	157	82	7.72E- 04	0.8900
		Median	115	71	3.35E- 04	0.9321
		SD	117	34	1.43E- 03	0.0946
VQZ A – 1b	7470	Min	56	37	8.31E- 07	0.4874
		Max	1191	285	1.74E- 02	0.9747
		Mean	135	78	6.12E- 04	0.9115
		Median	112	72	3.41E- 04	0.9379
		SD	76	27	8.79E- 04	0.0704
VQZ B – 1a	1445	Min	64	49	1.06E- 04	0.4753
		Max	1400	598	1.74E- 02	0.9712
		Mean	141	95	5.54E- 04	0.8960
		Median	108	82	2.94E- 04	0.9316
		SD	96	44	9.23E- 04	0.0837
VQZ B – 1b	5045	Min	63	42	8.47E- 05	0.4641
		Max	1135	418	2.77E- 02	0.9774
		Mean	146	80	9.36E- 04	0.9042
		Median	116	73	3.72E- 04	0.9340
		SD	94	29	1.41E- 02	0.0749
FGS – 1A	663	Min	71	46	1.46E- 04	0.5601
		Max	1298	328	2.98E- 02	0.9699
		Mean	142	93	8.57E- 04	0.8910
		Median	118	82	4.58E- 04	0.9116
		SD	99	25	1.98E- 03	0.0641
FGS – 1B	124	Min	23	18	4.35E- 06	0.7500
		Max	268	79	3.21E- 04	0.9445
		Mean	47	30	3.00E- 05	0.9220
		Median	38	27	1.38E- 05	0.9314
		SD	32	11	4.31E- 05	0.0312

6. Discussion

6.1. Gold characterization and metallurgical implications

Most of the gold in Cuiabá historically has been recovered by leaching after sulfide oxidation (Vitorino, 2017). The particle size distribution is a critical factor in leaching operations, which determines ultimate recovery and must be established based on the extent of mineral exposure and transport phenomena. As the major ore type in the

Cuiabá deposit is dominated by gold-bearing sulfide minerals hosted in BIF, exploiting vein-hosted occurrences such as the Veio de Quartzo (VQZ) orebody requires optimizations on ore recovery.

In the case of the mafic-hosted, vein-style ore sample, gold particles are mainly free in the quartz-carbonate matrix, though many particles are in direct contact or enclosed within diverse sulfide minerals, e. g. pyrite, chalcopyrite, sphalerite, galena and pyrrhotite. Vitorino (2017) suggested that although gold is mostly liberated during crushing of these vein-hosted ores, gold recovery would not be efficient using only gravimetric concentration because of the presence of small particles. On the other hand, the BIF-hosted ore sample FGS-1 reveals that gold is preferentially included in pyrrhotite, arsenopyrite and minor pyrite andor filling fine fractures in these sulfide minerals in stratabound replacement of iron carbonate layers. This relationship, along with the diversity of sulfides (e. g. galena, sphalerite) identified in the vein-hosted ore, shows that different ore types require different processing protocols to optimize gold recovery.

Because the data resolution is different for both samples under evaluation, it is not possible to compare mineralization styles regarding minimum gold size, volumes and size distributions. The in-situ volumetric information reveals the relationship between the cumulative percentage of grains from the largest (at 0%) to the smallest (at 100%), and the percentage of the total gold grade in both samples (Fig. 15). Approximately 40% of the largest particles account for 80% of the total gold volume of each case, with a minor percentage reflected by the numerous finer-grained particles. Given the exponential distribution of grain sizes, it is likely that there are particles smaller than the minimum size detected. However, as finer particles only account for a minor amount of the total gold volume, undetected particles are unlikely to have a major impact on ore grade (e.g. Kyle et al., 2008). In the finerresolution scan (FGS-1B, Fig. 15B), the distribution is skewed toward smaller particles representing less volume in comparison to sample FGS-1A. This effect is probably because the higher-resolution scan allowed more finer particles to be detected, increasing their representation but diminishing their volumetric importance, demonstrating the resolutiondependence of these curves.

The HRXCT results from the VQZ1 sample reveal the in-situ particle size distribution and 3-D mineral associations with various sulfide minerals, and thus represent supplementary information to geometallurgical processing. It has been shown that 3-D mineral liberation analysis based on X-ray Micro Tomography (XMT) is preferred over 2-D section analysis, which overestimates the extent of liberation (Miller et al., 2009). Additional HRXCT data processing and other studies are required to better assess gold liberation.

6.2. Structural analysis and implications to gold exploration

Gold in the vein-hosted, VQZ orebody sample occurs in shapes in which one shape factor (elongation or flatness) is larger than the other, as bladed, roller, oblate- and prolate-spheroid particles may be a result of preferential grain growth influenced by local strain. Although the identified particles in this sample are not geologically oriented, the dominant anisometric particles may be evidence of shearing of the fault-fill V1 vein system in the VQZ orebody. These veins are interpreted to have been emplaced during D1 shearing, considered as the main pathway for the gold-mineralizing hydrothermal fluids at Cuiabá by Vitorino et al. (2020).

The BIF-hosted FGS-1 sample reveals gold particles to be mainly associated with arsenopyrite and pyrrhotite and minor pyrite. Gold particles are located at arsenopyrite margins and filling its fractures (Fig. 10F). Some authors (e.g., Morey et al., 2008; Cook et al., 2013) suggest that during deformation gold incorporated within the structure of sulfide minerals may be remobilized and occupy such sites rather than being supplied at this time. These observations are consistent with those of Sayab et al. (2016), who also observed evidence in arsenopyrite for cycles of gold remobilization through 3-D data from HRXCT. The

Table 3Gold shape statistics from the Cuiabá deposit samples concerning r_{PSF} bigger than the particles' short axis.

Sample		Bladed	Discoid	Very oblate spheroid	Oblate spheroid	Sub-equant spheroid	Equant Spheroid	Prolate spheroid	Roller	Total of gold grains
VQZ A – 1a	>	16	0	5	29	148	51	82	31	362
	r_{PSF}	4.4%	0.0%	1.4%	8.0%	40.9%	14.1%	22.7%	8.6%	
	<	10	0	0	17	424	335	106	17	909
	r_{PSF}	1.1%	0.0%	0.0%	1.9%	46.6%	36.9%	11.7%	1.9%	
VQZA - 1b	>	24	0	3	83	1056	482	186	52	1886
	r_{PSF}	1.3%	0.0%	0.2%	4.4%	56.0%	25.6%	9.9%	2.8%	
	<	29	0	3	102	2577	2131	302	44	5188
	r_{PSF}	0.6%	0.0%	0.1%	2.0%	49.7%	41.1%	5.8%	0.8%	
VQZB-1a	>	11	0	3	10	53	12	46	15	150
	r_{PSF}	7.3%	0.0%	2.0%	6.7%	35.3%	8.0%	30.7%	10.0%	
	<	12	0	3	25	630	430	157	38	1295
	r_{PSF}	0.9%	0.0%	0.2%	1.9%	48.6%	33.2%	12.1%	2.9%	
VQZ B - 1b	>	28	0	5	39	326	96	192	34	720
	r_{PSF}	3.9%	0.0%	0.7%	5.4%	45.3%	13.3%	26.7%	4.7%	
	<	26	0	2	118	2226	1417	457	79	4325
	r_{PSF}	0.6%	0.0%	0.0%	2.7%	51.5%	32.8%	10.6%	1.8%	
FGS – 1A	>	1	0	0	0	1	1	0	0	3
	r_{PSF}	33.3%	0.0%	0.0%	0.0%	33.3%	33.3%	0.0%	0.0%	
	<	3	0	0	1	277	343	20	17	661
	r_{PSF}	0.5%	0.0%	0.0%	0.2%	42.0%	52.0%	3.0%	2.6%	
FGS - 1B	>	0	0	0	0	1	1	0	0	2
	r_{PSF}	0.0%	0.0%	0.0%	0.0%	0.8%	0.8%	0.0%	0.0%	
	<	0	0	0	1	38	67	11	5	122
	$r_{\rm PSF}$	0.0%	0.0%	0.0%	0.8%	30.6%	54.0%	8.9%	4.0%	

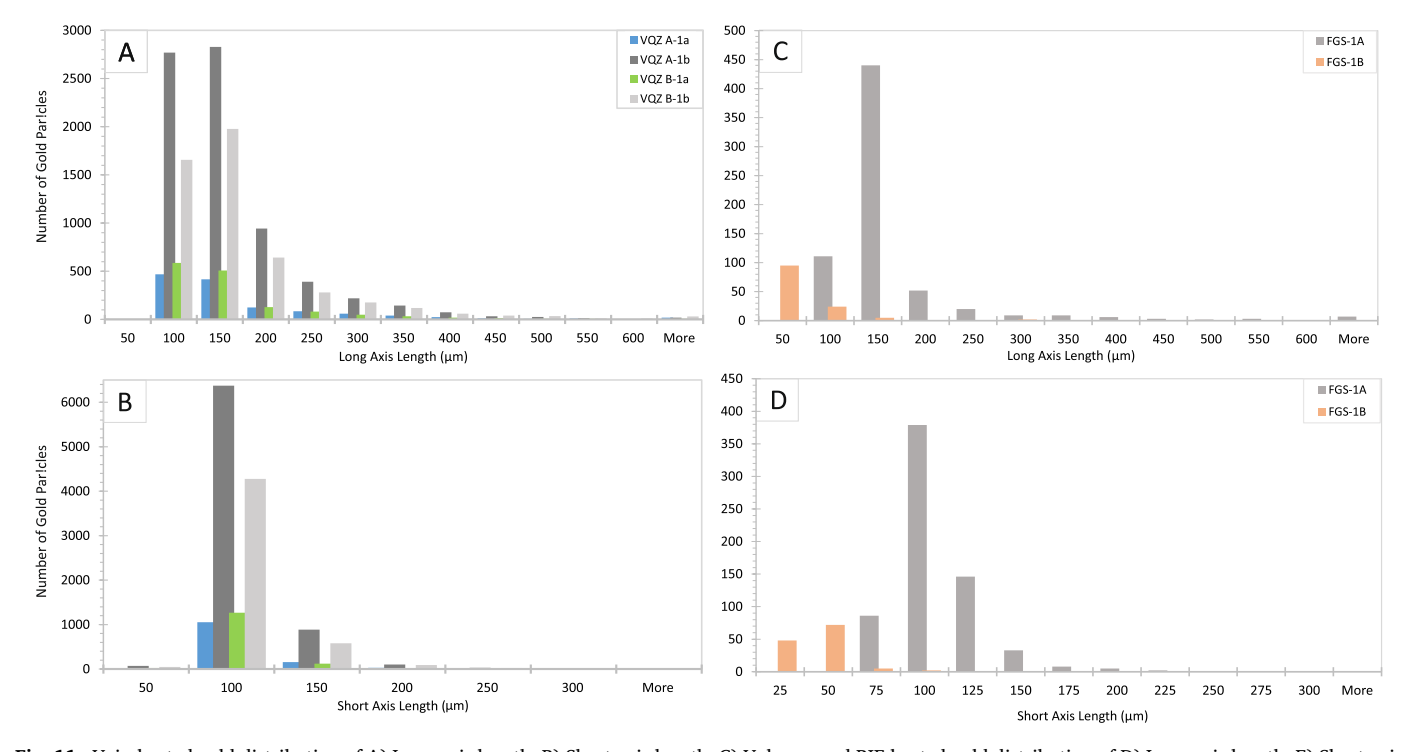


Fig. 11. Vein-hosted gold distribution of A) Long axis length, B) Short axis length, C) Volume; and BIF-hosted gold distribution of D) Long axis length, E) Short axis length, F) Volume.

preferred alignment of arsenopyrite, concordant to L_1 (Fig. 9), could suggest its formation during D1 following structural criteria established by Vitorino et al. (2020).

The in-situ measurements of gold particles within the BIF-ore sample also indicate a preferential distribution of major and minor axis orientations. The major axis girdle (Fig. 14A) may indicate that gold particles are located on a foliation plane that also contains L_1 , so a careful evaluation of structural orientations should be performed in a high-resolution scan of an oriented sample in order to better relate gold features to the structural controls at the Cuiabá deposit.

It is interesting to note that although gold is crystallized in the isometric system and its deformation takes place by dislocation, i. e. sliding of crystal planes over each other through movement along lattice defects (Hough et al., 2009), these results demonstrate that deformations D1 and D2 (Vitorino et al. 2020) may have a direct influence over the SEtrending gold particles.

Further studies on pyrrhotite-dominated ores are of great importance to provide additional evidence, as well as studies on gold remobilization mechanisms. These results provide valuable information on gold continuity and structural controls for mine-site exploration.

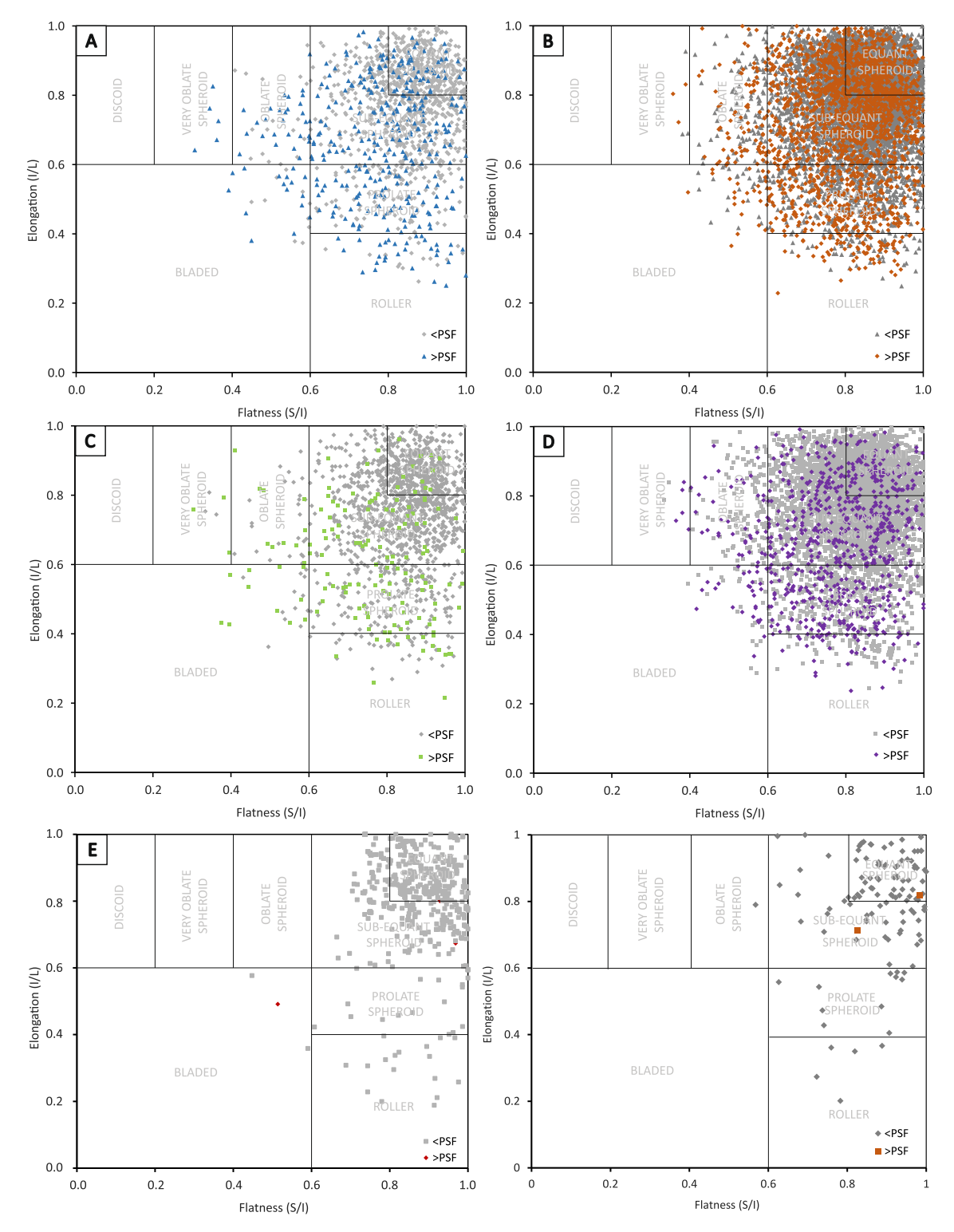


Fig. 12. Bivariate diagram (after Blott and Pye, 2008) for segmented gold particles regarding the particles with short axis below (gray) or above (colored) the r_{PSF} parameter resolution cutoff for reliable shape determination; see text for further explanation. Shape classification uses the combination of long (L), intermediate (I), and short (S) axial dimensions, with axes for particle elongation (I/L) and flatness (S/I). Particles may be bladed, discoid, roller, very prolate spheroid, prolate spheroid, oblate spheroid, sub-equant spheroid or equant spheroid. A) VQZ1 A-1a; B) VQZ1 B-1a; D) VQZ1 B-1b; E) FGS-1A; F) FGS-1B.

7. Conclusions

High-resolution X-ray computed tomography and PVB analysis provides unique three-dimensional data to characterize the in-situ nature of gold particles and associated minerals, revealing particle sizes, volumes, shapes, orientations, and textural relationships. In this paper, we have

discussed the metallurgical and exploration implications of this information at the world-class Archean Cuiabá orogenic gold deposit of the Quadrilátero Ferrífero province, comparing the differences between BIF-hosted and vein-hosted gold ores. The major findings can be summarized

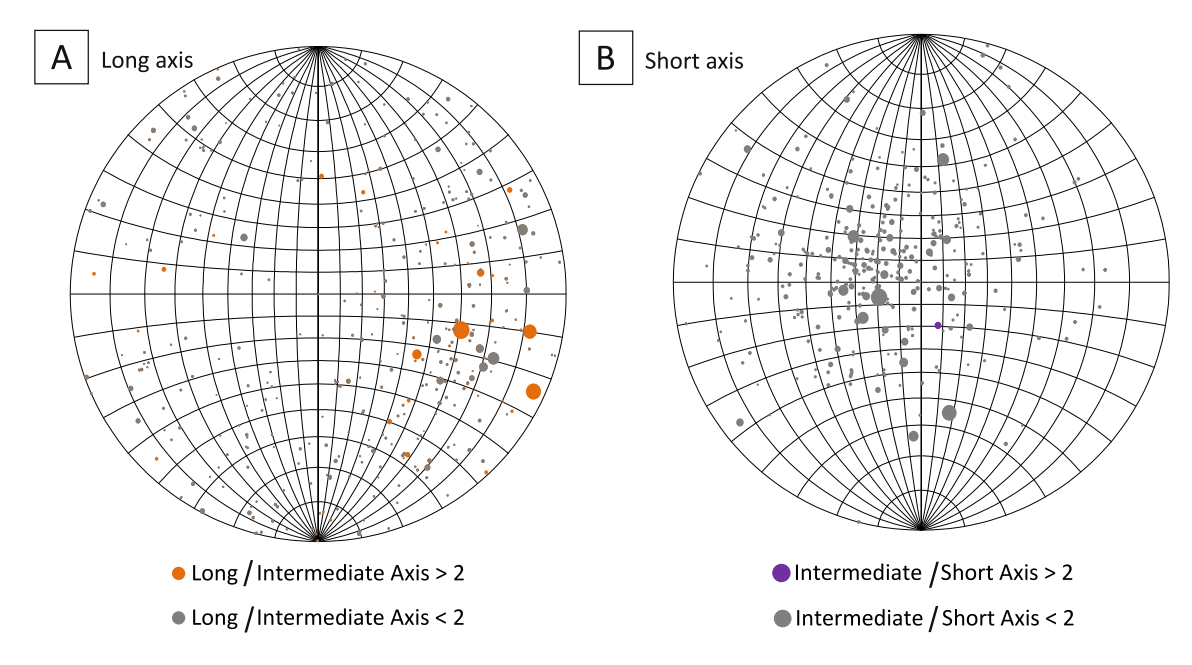


Fig. 13. Bubble charts on equal-angle lower hemisphere projections of long (A) and short axis orientations (B) in sample FGS-1A, with colors according to criteria for reliable (colored) or unreliable (gray) orientation determination and bubble sizes scaled according to gold particle volumes. Coarse particles display consistent clustering, whereas finer particles are dispersed.

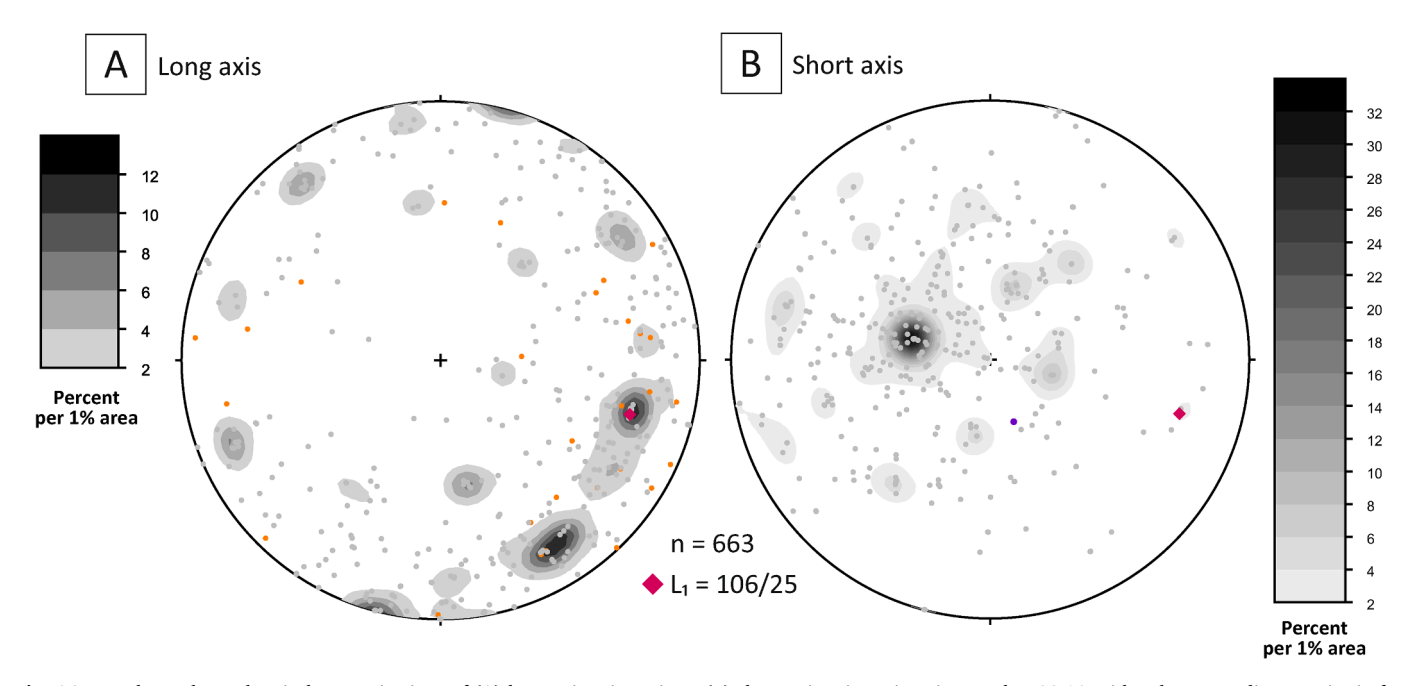


Fig. 14. Equal-area lower hemisphere projections of (A) long axis orientations, (B) short axis orientations in sample FGS-1A with colors according to criteria for reliable (colored) or unreliable (gray) orientation determination. Contours calculated through 1% Area method. Orientations do not correspond to true geological coordinates. The intersection lineation L_1 (106/25) is marked as a red diamond. (For interpretation of the references to color in this figure legend, the reader is referred to the web version of this article.)

- i. Gold occurrence: Gold particles in the mafic-hosted, vein-style ore, are mainly free in the quartz-carbonate matrix, although many particles are in direct contact or enclosed in diverse sulfide minerals, whereas the BIF-hosted ore reveals that gold is preferentially included in pyrrhotite, arsenopyrite and minor pyrite and/or filling fine fractures in these sulfide minerals.
- ii. Gold particle shape, size, and distribution: For both mineralization styles, finer gold particles appear to be more equant due to blurring effects. In addition, for both samples the largest particles
- account for the greatest amount of gold volume, so that finer particles are likely to have a minor impact on ore grade.
- iii. Vein-hosted (VQZ1) particle shape: The dominant anisometric gold particles in VQZ1, vein-style ore, may be a result of preferential grain growth influenced by local strain. Although the sample is not geologically oriented, the dominant anisometry may be evidence of shearing of the fault-fill V1 vein system in the VQZ orebody.
- iv. BIF-hosted (FGS-1) mineral orientations: The preferred alignment of arsenopyrite in the FGS-1, BIF-hosted ore, is concordant to the

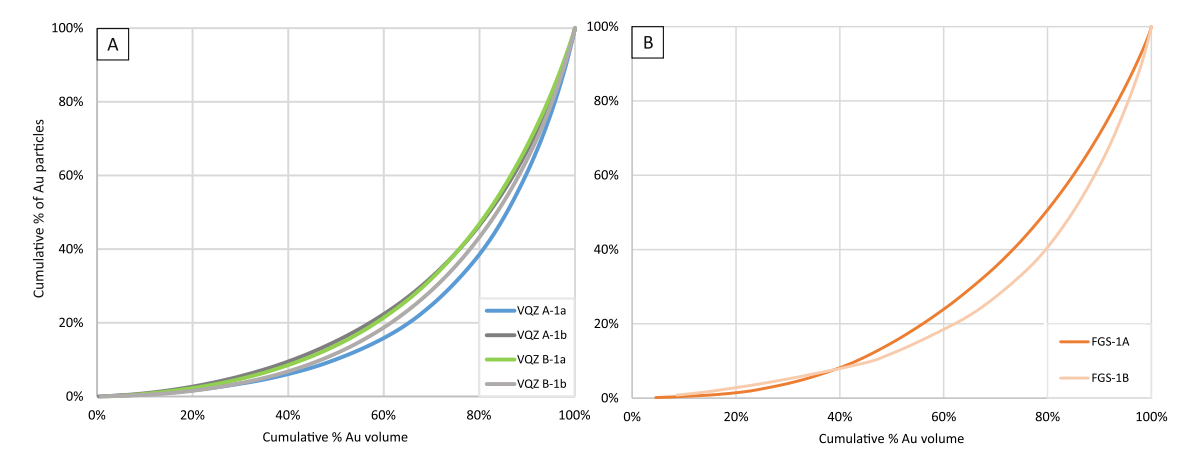


Fig. 15. Cumulative percentage of gold particles from the largest (at 0%) to the smallest (at 100%) contributing to the cumulative gold concentration on samples (A) VOZ1 A-1a, VOZ1 B-1a, VOZ1 B-1a, VOZ1 B-1b, and (B) FGS-1A and FGS-1B.

intersection and mineral lineation L_1 and must be related to D1 or D2 tectonic foliation planes. The location of gold in arsenopyrite fractures may be evidence that gold has been exsolved from the crystal structure and remobilized along secondary crystal fractures. Also, gold particles' long axis orientations indicate that the particles are oriented along a plane that contains the intersection lineation L_1 .

Declaration of Competing Interest

The authors declare that they have no known competing financial interests or personal relationships that could have appeared to influence the work reported in this paper.

Acknowledgments

This study was made possible by the Minas Mundi program, an exchange partnership of the Federal University of Minas Gerais with The University of Texas at Austin that allowed the first author to take part of her undergraduate studies at the latter. We are grateful for the support by AngloGold Ashanti Brazil (AGA) in providing samples, and all other research expenditures and support, especially R.F. Cota, J.H.C. Canela and P.D. Barroso, along with the former AGA's geologists A.L. Vitorino and F.L.S.P. Villanova. Thanks to G.A. Silveira for the discussions on structural geology. Our thanks are also due to The University of Texas at Austin HRXCT Facility (UTCT), especially M. Colbert, and to the Geosciences Institute at the Federal University of Minas Gerais. UTCT is supported by National Science Foundation grant EAR-1762458 to R.A.K; L.M.L. is a recipient of a research grant by the Conselho Nacional de Pesquisa Científica e Tecnológica-CNPq, Brazil.

Appendix A. Supplementary data

Supplementary data to this article can be found online at https://doi.org/10.1016/j.oregeorev.2021.104584.

References

Akin, S., Kovscek, A.R., 2003, Computed tomography in petroleum engineering research: Geological Society London, Special Publication, v. 215, p. 23–38.

Almeida, F.F.M., 1967. Evolução tectônica do centro-oeste brasileiro no Proterozóico Superior. Annaes Academia Brasileira de Geociências 7, 349–364.

Babinski, M., Chemale Jr., F., Van Schmus, W.R., 1995, The Pb/Pb age of the Minas Supergoup carbonate rocks, Quadrilátero Ferrífero, Brazil: Precambrian Research, v. 72, p. 235–245.

Baltazar, O.F., Lobato, L.M., 2020, Structural evolution of the Rio das Velhas Greenstone Belt, Quadrilátero Ferrífero, Brazil: Influence of Proterozoic orogenies on its Western Archean Gold Deposits: Minerals, 10, v. 983, p. 1-38. Baltazar, O.F., Zucchetti, M., 2007. Lithofacies associations and structural evolution of the Archean Rio das Velhas greenstone belt, Quadrilátero Ferrífero, Brazil: a review of the setting of gold deposits. Ore Geol. Rev. 32 (3-4), 471–499.

Cabral, A.R., Zeh, A., Koglin, N., Seabra Gomes, A.A., Viana, D.J., Lehmann, B., 2012. Dating the Itabira iron formation, Quadrilátero Ferrifero of Minas Gerais, Brazil, at 2.65 Ga: depositional U-Pb age of zircon from a metavolcanic layer. Precambr. Res. 204-205, 40-45.

Cnudde, V., Boone, M.N., 2013. High-resolution X-ray computed tomography in geosciences: a review of the current technology and applications. Earth Sci. Rev. 123, 1–17.

Cook, N.J., Ciobanu, C.L., Meria, D., Silcock, D., Wade, B., 2013. Arsenopyrite-pyrite association in an orogenic gold ore: Tracing mineralization history from textures and trace elements. Econ. Geol. 108 (6), 1273–1283.

Costa, M., 2000. Estudo de isótopos de carbono e oxigênio e caracterização petrográfica do minério da Mina Cuiabá: Unpusblished M. Sc. thesis. Universidade Federal de Minas Gerais, Belo Horizonte, Brazil.

Denison, C., Carlson, W.D., 1997. Three-dimensional quantitative textural analysis of metamorphic rocks using high-resolution computed X-ray tomography: Application to natural samples. J. Metamorph. Geol. 15, 45–57.

Denison, C., Carlson, W.D., Ketcham, R.A., 1997. Three-dimensional quantitative textural analysis of metamorphic rocks using high-resolution computed X-ray tomography. J. Metamorph. Geol. 15, 29–44.

Dhawan, N., Safarzadeh, M.S., Miller, J.D., Moats, M.S., Rajamani, R.K., Lin, C.-L., 2012. Recent advances in the application of X-ray computed tomography in the analysis of heap leaching systems. Miner. Eng. 35, 75–86.

Dorr, J.V.N., 1969, Physiographic, stratigraphic, and structural development of the Quadrilátero Ferrífero, Minas Gerais, Brazil: U.S. Geological Survey, v. 614 (A), p. 110.

Endo I., Galbiatti H. F., Delgado C. E. R., Oliveira M. M. F. de, Zapparoli A. de C., Moura L. G. B. de, Peres G. G., Oliveira A. H. de, Zavaglia G., Danderfer F. A., Gomes C. J. S., Carneiro M. A., Nalini Jr. H. A., Castro P de T. A., Suita M. T. de F., Seixas L. A. R., Tazava E., Lana C. de C., Martins-Neto M. A., Martins M. de S., Ferreira F. F. A., Franco A. P., Almeida L. G., Rossi D. Q., Angeli G., Madeira T. J. A., Piassa L. R. A., Mariano D. F., Carlos D. U., 2019a, Mapa geológico do Quadrilátero Ferrífero, Minas Gerais, Brasil, Escala 1:150.000: Ouro Preto, Departamento de Geologia, Escola de Minas – UFOP – Centro de Estudos Avançados do Quadrilátero Ferrífero.

Endo I., Delgado C. E. R. Oliveira M. M. F. de, Zapparoli A. de C., Carlos D. U., Galbiatti H. F., Castro P. de T. A., Suita M. T. de F., Barbosa M. S. C., Lana C. E., Moura L. G. B. de., 2019b, Estratigrafia e Arcabouço Estrutural do Quadrilátero Ferrífero: Nota Explicativa do Mapa Geológico do Quadrilátero Ferrífero, Minas Gerais, Brasil, Escala 1:150.000: Ouro Preto, Departamento de Geologia da Escola de Minas – UFOP – Centro de Estudos Avançados do Quadrilátero Ferrífero.

Farina, F., Albert, C., Lana, C., 2015. The Neoarchean transition between medium-and high-K granitoids: clues from the Southern São Francisco Craton (Brazil). Precambr. Res. 266, 375–394

Fernandes, R.C., Endo, I., Pereira, R.M.P., Rivarola, I., Souza, J.C., 2016, Geologia e Evolução Estrutural do Depósito Aurífero Cuiabá: Novas Perspectivas para a Exploração Mineral, Seção Pôster: VII Simpósio Brasileiro de Exploração Mineral, SIMEXMIN, Ouro Preto, Brazil.

Godel, B., 2013. High-resolution X-ray computed tomography and its application to ore deposits: from data acquisition to quantitative three-dimensional measurements with case studies from Ni–Cu–PGE deposits. Econ. Geol. 108 (8), 2005–2019.

Godel, B., Barnes, S.-J., Maier, W.D., 2006, 3D distribution of sulphide minerals in the Merensky reef (Bushveld Complex, South Africa) and the J-M reef (Stillwater Complex, USA) and their relationship to microstructures using X-Ray computed tomography: Journal of Petrology, v. 47, p. 1853–1872.

Godel, B., Barnes, S.J., Austin, P., Gürer, D.M., Fiorentini, M.L., 2013. Chromite in komatiites: 3D morphologies and sizes with implications for crystallization mechanisms: Contribution to. Mineral. Petrol. 165, 173–189.

Godel, B., Barnes, S.J., Barnes, S.-J., Maier, W.D., 2010. Platinum ore in 3D: Insights from high-resolution X-ray computed tomography. Geology 38, 1127–1130.

- Goldfarb, R.J., Groves, D.I., 2015. Orogenic gold: common or evolving fluid and metal sources through time. Lithos 233, 2–26.
- Groves, D.I., Goldarb, R.J., Gebre-Mariam, M., Hagemann, S.G., Robert, F., 1998. Orogenic gold deposits: a proposed classification in the context of their crustal distribution and relationship to other gold deposit types. Ore Geol. Rev. 13 (1-5), 7–27.
- Hanna, R.D., Ketcham, R.A., 2017. X-ray computed tomography of planetary materials: a primer and review of recent studies. Chemie der Erde Geochemistry 77 (4), 547–572.
- Herz, N., 1970, Gneissic and igneous rocks of the Quadrilátero Ferrifero, Minas Gerais, Brazil: United States Geological Survey Professional Paper, v. 641-B, 58p.
- Hezel, D.C., Elangovan, P., Viehmann, S., Howard, L., Abel, R.L., Armstrong, R., 2013. Visualization and quantification of CV chondrite petrography using microtomography. Geochim. Cosmochim. Acta 116, 33–40.
- Hough, R.M., Butt, C.R.M., Fischer-Buhner, J., 2009. The crystallography, metallography and composition of gold. Elements 5 (5), 297–302.
- Huddlestone-Holmes, C.R., Ketcham, R.A., 2010. An X-ray computed tomography study of inclusion trail orientation in multiple porphyroblasts from a single sample. Tectonophysics 480, 305–320.
- Jerram, D.A., Davis, G.R., Mock, A., Charrier, A., Marsh, B.D., 2010, Quantifying 3D crystal populations, packing and layering in shallow intrusions: a case study from the basement sill, Dry Valleys, Antarctica: Geosphere, v. 6, p. 537–548.
- Jerram, D.A., Mock, A., Davis, G.R., Field, M., Brown, R.J., 2009. 3D crystal size distributions: a case study on quantifying olivine populations in kimberlites. Lithos 112, 223–235.
- Ketcham, R.A., 2005. Computational methods for quantitative analysis of threedimensional features in geological specimens. Geosphere 1 (1), 32–41.
- Ketcham, R.A., Carlson, W.D., 2001. Acquisition, optimization and interpretation of X-ray computed tomographic imagery: applications to the geosciences. Comput. Geosci. 27 (4), 381–400.
- Ketcham, R.A., Hildebrandt, J., 2014. Characterizing, measuring, and utilizing the resolution of CT imagery for improved quantification of fine-scale features. Nucl. Instrum. Methods Phys. Res. B 324, 80–87.
- Ketcham, R.A., Mote, A.S., 2019. Accurate measurement of small features in X-ray CT data volumes, demonstrated using gold grains: Journal of Geophysical Research: Solid. Earth 124 (4), 3508–3529.
- Kresse, C., Lobato, L.M., Hagemann, S.G., Figueiredo e Silva, R.C., 2018. Sulfur isotope and metal variations in sulfides in the BIF-hosted orogenic Cuiabá gold deposit, Brazil: implications for the hydrothermal fluid evolution. Ore Geol. Rev. 98, 1–27.
- Kresse, C., Lobato, L.M., Figueiredo e Silva, R.C., Hagemann, S.G., Banks, D., Vitorino, A. L.A., 2020. Fluid signature of the shear zone–controlled Veio de Quartzo ore body in the world-class BIF-hosted Cuiabá gold deposit, Archaean Rio das Velhas greenstone belt, Brazil: a fluid inclusion study. Mineralium Deposita 55 (7), 1441–1466.
- Kyle, J.R., Ketcham, R.A., 2003, In-situ distribution of gold in ores using high resolution X-ray computed tomography: Economic Geology, v. 98, p. 1697–1701.
- Kyle, J.R., Ketcham, R.A., 2015. Application of high resolution X-ray computed tomography to mineral deposit origin, evaluation, and processing. Ore Geol. Rev. 65, 821–839.
- Kyle, J.R., Mote, A.S., Ketcham, R.A., 2008. High resolution X-ray computed tomography studies of Grasberg porphyry Cu–Au ores. Miner. Deposita 43, 519–532.
- Lana, C., Alkmin, F.F., Armstrong, R., Scholz, R., Romano, R., Nalini Jr., H.A., 2013. The ancestry and magmatic evolution of Archaean TTG rocks of the Quadrilátero Ferrífero province, southeast Brazil. Precambr. Res. 231, 157–173.
- Le Roux, S.G., Plessis, A.D., Rozendaal, A., 2015. The quantitative analysis of tungsten ore using X-ray micro CT: Case study. Comput. Geosci. 85, 75–80.
- Liu, P.-P., Zhou, M.-F., Chen, W.T., Boone, M., Cnudde, V., 2014, Using multiphase solid inclusions to constrain the origin of the Baima Fe–Ti–(V) oxide deposit, SW China, J. Petrol., v. 55, p. 951–976.
- Lobato, L.M., Ribeiro Rodrigues, L.C., Vieira, F.W.R., 2001b, Brazil's premier gold province, part II: geology and genesis of gold deposits in the Archean Rio das Velhas greenstone belt, Quadrilátero Ferrifero: Mineralium Deposita, v. 36, p. 249–277.
- Lobato, L.M., Ribeiro Rodrigues, L.C., Zucchetti, M., Noce, C.M., Baltazar, O.F., da Silva, L., Pinto, C., 2001b. Brazil's premier gold province, part I: the tectonic, magmatic, and structural setting of the Archean Rio das Velhas greenstone belt. Quadrilátero Ferrífero: Mineralium Deposita 36 (3-4), 228–248.
- Lobato, L.M., Santos, J.O.S., McNaughton, N.J., Fletcher, I.R., Noce, C.M., 2007. U-Pb SHRIMP monazite ages of the giant Morro Velho and Cuiabá gold deposits, Rio das Velhas greenstone belt, Quadrilátero Ferrífero, Minas Gerais, Brazil. Ore Geol. Rev. 32 (3-4), 674–680.
- Lobato, L.M., Vieira, F.W.R., 1998. Styles of hydrothermal alteration and gold mineralization associated with the Nova Lima Group, Quadrilátero Ferrifero: Part II, the Archaean mesothermal gold-bearing hydrothermal system: Brazilian. J. Geol. 28, 355–366.
- Machado, N., Carneiro, M., 1992. U-Pb evidence of late Archean tectono-thermal activity in the southern S\u00e4o Francisco shield, Brazil. Can. J. Earth Sci. 29 (11), 2341–2346.
- Machado, N., Schrank, A., Abreu, F.R., Knauer, L.G., Almeida-Abreu, P.A., 1989,
 Resultados preliminares da geocronologia U/Pb na Serra do Espinhaço Meridional.
 In: Anais do V Simp. Geol. Minas Gerais, Belo Horizonte, p. 171-174.
- Machado, N., Schrank, A., Noce, C.M., Gauthier, G., 1996. Ages of detrital zircon from Archean-Paleoproterozoic sequences: Inplications for Green-stone Belt setting evolution of a Transamazonian foreland basin in Quadrilátero Ferrifero, southeast Brazil. Earth Planet. Sci. Lett. v. 141, 259–276.
- Marshak, S., Alkmim, F.F., 1989. Proterozoic contraction/extension tectonics of the Southern S\u00e4o Francisco Region. Minas Gerais, Brazil: Tectonics 8 (3), 555-571.
- Mauk, J.L., Kyle, J.R., Simpson, M.P., Atkinson, P., 2006, Ore mineralogy of the BM37 shoot of the Karangahake deposit, New Zealand: Proceedings, 39th Annual

- Conference of the New Zealand Branch of the Australian Institute of Mining and Metallurgy, p. 233–242.
- Mees, F., Swennen, R., VanGeet, M., Jacobs, P., 2003, Applications of X-ray computed tomography in the geosciences: Geological Society London, Special Publication 215.
- Merinero, R., Ortega, L., Lunar, R., Piña, R., Cárdenes, V., 2019. Framboidal chalcopyrite and bornite constrain redox conditions during formation of their host rocks in the copper stratabound mineralization of Picachos, north-central Chile. Ore Geol. Rev. 112, 103037. https://doi.org/10.1016/j.oregeorev.2019.103037.
- Miller, J.D., Lin, C.L., Garcia, C., Arias, H., 2003. Ultimate recovery in heap leaching operations as established from mineral exposure analysis by X-ray microtomography. Int. J. Miner. Process. 72 (1-4), 331–340.
- Miller, J.D., Lin, C.L., Hupka, L., Al-Wakeel, M.I., 2009. Liberation-limited grade/ recovery curves from X-ray micro CT analysis of feed material for the evaluation of separation efficiency. Int. J. Miner. Process. 93 (1), 48–53.
- Moreira, H., Lana, C., Nalini, H.A., 2016. The detrital zircon record of an Archean convergent basin in the southern São Francisco Craton, Brazil. Precambr. Res. 275, 84–99.
- Morey, A.A., Tomkins, A.G., Bierlein, F.P., Weinberg, R.F., Davidson, G.J., 2008. Bimodal distribution of gold in pyrite and arsenopyrite: Example from the Archean Boorara and Bardoc shear systems, Yilgarn craton, western Australia. Econ. Geol. 103, 599-614.
- Mote, A.S., Kyle, J.R., Ketcham, R.A., Melker, M.D., Jahraus, M.J., Brown, T.R., Wawrzyniec, T.F., 2005, High resolution X-ray computed tomography investigations of high-grade gold ore zones in the Cripple Creek District, Colorado. In: Rhoden, H. N., et al. (Eds.), Geological Society of Nevada Symposium 2005: Window to the World Symposium, Reno, Nevada, p. 1169–1175.
- Noce, C.M., Tassinari, C., Lobato, L.M., 2007. Geochronological framework of the Quadrilátero Ferrífero, with emphasis on the age of gold mineralization hosted in Archean greenstone belts. Ore Geol. Rev. 32, 500–510.
- Open Stereo, 2010: http://igc.usp.br/openstereo/. Accessed 15 June 2020.
- Phillips, G.N., Groves, D.I., Martyn, J.E., 1984. An epigenetic origin for Archean banded iron-formation-hosted gold deposits. Econ. Geol. 79, 162–171.
- Reyes, F., Lin, Q., Udoudo, O., Dodds, C., Lee, P.D., Neethling, S.J., 2017. Calibrated X-ray micro-tomography for mineral ore quantification. Miner. Eng. 110, 122–130.
- Ribeiro Rodrigues, L.C., 1998, Gold in Archaen banded iron formation of the Quadrilátero Ferrífero, Minas Gerais, Brazil – The Cuiabá Mine: Unpublished Ph.D. thesis, Aachen University of Technology. Augustinus Verlag, Aachener Geowissenschaftliche Beiträge, Band 27, 264 p.
- Ribeiro Rodrigues, L.C., de Oliveira, C.G., Friedrich, G., 2007. The Archean BIF-hosted Cuiabá Gold deposit Quadrilátero Ferrífero, Minas Gerais, Brazil. Ore Geol. Rev. 32, 543–570
- Ribeiro Rodrigues, L.C., Friedrich, G., Oliveira, C.G., Vieira, F.W.R., Callegari, L.A., Biasi, E.E., 1996a, Ore textures and structures of the Archean banded iron formation Cuiabá gold deposit, Iron Quadrangle, Minas Gerais, Brazil: Zentalblatt für Geologie und Paläontologie Teil, v. I, p. 627–642.
- Sayab, M., Suuronen, J.-P., Hölttä, P., Aerden, D., Lahtinen, R., Kallonen, A.K., 2016. High resolution X-ray computed microtomography: A holistic approach to metamorphic fabric analyses. Geology 43, 55-58.
- Sena, N. C., 2020, Modelo genético e paleoambiental de formações ferriferas, metacherts e rochas metavulcânicas, depósito Cuiabá, greenstone belt Rio das Velhas, Quadrilátero Ferrifero, Minas Gerais, Brasil: Unpublished M.Sc. thesis, Belo Horizonte, Brazil, Universidade Federal de Minas Gerais, 125 p.
- Van Geet, M., Swennen, R., Wevers, M., 2000. Quantitative analysis of reservoir rocks by micro focus X-ray computerized tomography. Sed. Geol. 132 (1–2), 25–36.
- Vial, D.S., 1980. Mapeamento Geológico do Nivel 3 da mina de Cuiabá: Internal Report. Mineração Morro Velho S. A, Nova Lima, Brazil.
- Vial, D.S., 1988a, Mina de ouro de Cuiabá, Quadrilátero Ferrífero, Minas Gerais. In: Schobenhaus-Filho, C., Coelho, C.E.S. Metais básicos não ferrosos, ouro e alumínio: Departamento Nacional da Produção Mineral/Campanhia, Vale Rio Doce, Brasília, p. 413-419.
- Vial, D.S., DeWitt, E., Lobato, L.M., Thorman, C.H., 2007. The geology of the Morro Velho gold deposit in the Archean Rio das Velhas greenstone belt, Quadrilátero Ferrífero, Brazil. Ore Geol. Rev. 32, 511–542.
- Vieira, F.W.R., 1992. Geologia da Mina de Cuiabá, Níveis 03 e 04: Internal Report. Mineração Morro Velho S. A, Nova Lima, Brazil, p. 23.
- Vieira, F.W.R., 1988. Caracterização petrográfica e mineralógica do minério do corpo galinheiro extensão, open pit Cuiabá: Internal Report. Mineração Morro Velho S. A, Nova Lima, Brazil, p. 6.
- Vieira, F.W.R., 1991a, Textures and processes of hydrothermal alteration and mineralization in the Nova Lima Group, Minas Gerais, Brazil: In: Ladeira, E.A. (Ed.), Brazil Gold's, Balkema, Roterdam, p. 319–327.
- Vieira, F.W.R., 1991b, Petrologia e litogeoquímica do Setor W do "Greenstone belt" Rio das Velhas, MG: Simpósio internacional de Geologia do Grupo AMSA, Nova Lima, Mineração Morro Velho Internal Report. 24 p.
- Vitorino, A.L.A., 2017, Mineralização aurífera associada aos veios quartzo-carbonáticos hospedados na unidade máfica basal da Jazida Cuiabá, Greenstone Belt Rio das Velhas, Quadrilátero Ferrífero, Minas Gerais, Brasil: Unpublished M.Sc. thesis, Belo Horizonte, Brazil, Universidade Federal de Minas Gerais.
- Vitorino, A.L.A., 2020. Shear-zone-related gold mineralization in quartz-carbonate veins from metamafic rocks of the BIF-hosted world-class Cuiaba deposit, Rio das Velhas

greenstone belt, Quadrilatero Ferrifero, Brazil: Vein classification and structural

control. Ore Geol. Rev. 127, 103789.

Vukmanovic, Z., Barnes, S.J., Reddy, S., Godel, B., Fiorentini, M.L., 2013. Microstructure in chromite crystals of the Merensky reef (Bushveld Complex, South Africa). Contrib. Miner. Petrol. 165, 1031–1050.

Wright, K.A., 2017, Correlating Cu-Fe sulfides and Au mineralization in the Ertsberg-Grasberg District of Papua, Indonesia using volumetric analysis and trace element geochemistry: Unpublished M.Sc. thesis, Austin, United States of America, University of Texas at Austin, 273 p.